Disruption of recombination machinery alters the mutational landscape in plant organellar genomes

Gus Waneka[1,a], Amanda K. Broz[1,a], Forrest Wold-McGimsey[1], Yi Zou[2], Zhiqiang Wu[2], Daniel B. Sloan[1]

[1]Department of Biology, Colorado State University, Fort Collins, Colorado, USA.
[2]Guangdong Laboratory for Lingnan Modern Agriculture, Genome Analysis Laboratory of the Ministry of Agriculture, Agricultural Genomics Institute at Shenzhen, Chinese Academy of Agricultural Sciences, Shenzhen, Guangdong 518120, China.

[a]These authors contributed equally to this work.

ABSTRACT

Land plant organellar genomes have extremely low rates of point mutation yet also experience high rates of recombination and genome instability. Characterizing the molecular machinery responsible for these patterns is critical for understanding the evolution of these genomes. While much progress has been made towards understanding recombination activity in land plant organellar genomes, the relationship between recombination pathways and point mutation rates remains uncertain. The organellar targeted *mutS* homolog MSH1 has previously been shown to suppress point mutations as well as non-allelic recombination between short repeats in *Arabidopsis thaliana*. We therefore implemented high-fidelity Duplex Sequencing to test if other genes that function in recombination and maintenance of genome stability also affect point mutation rates. We found small to moderate increases in the frequency of single nucleotide variants (SNVs) and indels in mitochondrial and/or plastid genomes of *A. thaliana* mutant lines lacking *radA*, *recA1*, or *recA3*. In contrast, *osb2* and *why2* mutants did not exhibit an increase in point mutations compared to wild type (WT) controls. In addition, we analyzed the distribution of SNVs in previously generated Duplex Sequencing data from *A. thaliana* organellar genomes and found unexpected strand asymmetries and large effects of flanking nucleotides on mutation rates in WT plants and *msh1* mutants. Finally, using long-read Oxford Nanopore sequencing, we characterized structural variants in organellar genomes of the mutant lines and show that different short repeat sequences become recombinationally active in different mutant backgrounds. Together, these complementary sequencing approaches shed light on how recombination may impact the extraordinarily low point mutation rates in plant organellar genomes.

INTRODUCTION

Nearly all eukaryotes rely on genes encoded in endosymbiotically derived mitochondrial genomes (mtDNAs) for cellular respiration. Plants and algae additionally rely on the endosymbiotically derived plastid genome (cpDNA) for photosynthesis. In several regards, land plant organellar genome evolution is atypical compared to mtDNA evolution in other eukaryotes (Smith and Keeling 2015). For one, plant organellar genomes have low nucleotide substitution rates relative to those in plant nuclear genomes and to those of many other eukaryotic mtDNAs. The low substitution rates of plant organellar genomes extend even to synonymous sites, which likely experience very little purifying selection, suggesting that the cause of the low evolutionary rates is a low underlying point mutation rate (Wolfe *et al.* 1987; Drouin *et al.* 2008).

Compared to the small mtDNAs typical in metazoans (generally below 20 kb) and in algae and fungi (with sizes ranging from approximately 13 to 96 kb and ~20 to 235 kb, respectively), land plant mtDNAs are much larger with sequenced mtDNAs averaging 395 kb (Wu *et al.* 2022) and a known range extending from 70 kb to over 10 Mb (Boore 1999; Sloan *et al.* 2012; Skippington *et al.* 2017; Gualberto and Newton 2017; Sandor *et al.* 2018; Chen *et al.* 2019). Very little of this size variation stems from differences in coding capacity, as plant mtDNAs generally contain a subset of the same 41 protein-coding genes (Mower *et al.* 2012). Instead, the fluctuations in total mtDNA size primarily result from the acquisition and loss of noncoding DNA. Even closely related species possess very little shared noncoding sequence (Kubo and Newton 2008; Skippington *et al.* 2017). For example, a comparative analysis of the mtDNAs of two species within the Brassicaceae, *Arabidopsis thaliana* (367 kb) and *Brassica napus* (222 kb), revealed a mere 78 kb of shared sequence, most of which is coding (Handa 2003). Though size variation of cpDNAs is less extreme than in plant mtDNAs, variation still exists with 98.7% of sequenced land plant cpDNAs ranging from 100-200 kb in size (Xiao-Ming *et al.* 2017).

Plant organellar genomes also experience exceptionally high rates of structural mutation and rearrangement (Palmer and Herbon 1988). As a result, there is virtually no conservation of synteny between plant mtDNAs, as evidenced by the extensive

rearrangements in alignments of mtDNAs from Col-0 and Ler ecotypes of *A. thaliana* (Stupar *et al.* 2001; Huang *et al.* 2005; Davila *et al.* 2011; Pucker *et al.* 2019; Zou *et al.* 2022). The structural instability in plant mtDNAs is partly explained by the presence of repeats of various lengths, which recombine frequently and give rise to multiple isomeric subgenomes with circular, linear and/or branched structures (Palmer and Herbon 1988; Alverson *et al.* 2011; Wynn and Christensen 2019). In fact, plant mtDNAs lack origins of replication, which help coordinate genome replication in many other eukaryotes, and are instead thought to replicate through break induced recombination (Gualberto and Newton 2017; Chevigny *et al.* 2020). Land plant cpDNAs are also recombinationally active but usually remain structurally conserved, albeit with some significant exceptions (Smith and Keeling 2015).

The seemingly disparate features of plant organellar evolution (i.e. high rates of recombination and low rates of point mutation) may be unified through a DNA repair mechanism reliant on recombination (Christensen 2014). This hypothesized mechanism hinges on the activity of the *mutS* homolog MSH1 (Abdelnoor *et al.* 2003), which is dual-targeted to mitochondria and plastids and has long been known to suppress non-allelic recombination between intermediate-sized repeats (50 to 600 bps) in the *A. thaliana* mtDNA (Martínez-Zapater *et al.* 1992; Arrieta-Montiel *et al.* 2009; Davila *et al.* 2011; Zou *et al.* 2022). Plant MSH1 is a chimeric fusion of a *mutS* gene with a GIY-YIG endonuclease domain (Abdelnoor *et al.* 2006) that has been proposed to introduce breaks in organellar DNA at the site of mismatches, which would then be repaired through homologous recombination (Christensen 2014, 2018; Ayala-García *et al.* 2018; Broz *et al.* 2022). Assays conducted on purified MSH1 *in vitro* have found that it has DNA binding and endonuclease activity with affinity for displacement loops (D-loops) (Peñafiel-Ayala *et al.* 2023).

We previously found support for a MSH1-mediated link between recombination and point mutations by using a high-fidelity Duplex Sequencing technique (Kennedy *et al.* 2014) to screen for single nucleotide variants (SNVs) and indels in *msh1* mutants (Wu *et al.* 2020). In that study, we also included a panel of mutants lacking functional copies of other genes involved in organellar DNA replication, recombination, and/or repair, including the

recombination protein RECA3, the paralogous organellar DNA polymerases POLIA and POLIB, and the glycosylases UNG, FPG, and OGG (Wu *et al.* 2020). Compared to wild type (WT) lines, *msh1* mutants incurred SNVs at a ~10-fold increase in mtDNA and a ~100-fold increase in cpDNA, and increases in indel frequencies were even greater. In contrast, *recA3* mutants showed only a small (and marginally significant) increase in mtDNA mutation, and none of the other lines in the mutant panel showed a significant increase in SNVs or indels compared to WT plants (Wu *et al.* 2020).

Here, we investigate additional organellar genome repair proteins (WHY2, RADA, RECA1, OSB2) known to play a role in the suppression of non-allelic recombination in the *A. thaliana* organellar genomes. WHY2 is a mitochondrially targeted whirly protein that binds single-stranded DNA to inhibit recombination between small repeated sequences via micro-homology mediated end joining (MMEJ) (Cappadocia *et al.* 2010) and is also the most abundant protein in mitochondrial nucleoids (as measured in *A. thaliana* cell culture; Fuchs *et al.* 2020). RADA is a dual-targeted DNA helicase, which has been shown to accelerate the processing of recombination intermediates and promote mtDNA stability in *A. thaliana* (Chevigny *et al.* 2022). RECA1 is a plastid-targeted protein that has been proposed to act synergistically with plastid whirly proteins to promote plastid genome integrity either by facilitating polymerase lesion bypass or by reversing stalled replication forks (Rowan *et al.* 2010; Zampini *et al.* 2015). OSB2 is a plastid-targeted single-stranded DNA binding protein that has been shown to hamper microhomology-mediated end joining *in vitro* (García-Medel *et al.* 2021). Given that we previously saw a weak signal of increased mtDNA mutation in *recA3* mutants (Wu *et al.* 2020), we included another *recA3* mutant allele in this study. In addition to these newly generated mutant lines, we also present an extended analysis of Duplex Sequencing data from Wu *et al.* (2020) to understand how SNVs are distributed among genomic regions, strand (template vs. non-template) of genic regions, and trinucleotide contexts. Finally, we also performed long-read Oxford Nanopore sequencing on the mutant lines, allowing us to study structural mutations and rearrangements. Collectively, these analyses provide a detailed characterization of the

effects of numerous recombination-related genes on point mutations and structural variants in plant organellar genomes.

METHODS

Generation and analysis of Duplex Sequencing libraries for SNV and indel detection

We obtained seeds for *A. thaliana osb2*, *radA*, *recA1*, *recA3*, and *why2* mutants from the Arabidopsis Biological Resource Center (Table S1). The generation of Duplex Sequencing data from mutants and matched WT controls (including crossing, plant growth, organelle isolation, DNA extraction, and library preparation) closely followed our previously described protocols (Wu *et al.* 2020). For each gene of interest, homozygous mutants were used as the paternal pollinators in crosses against WT maternal plants, which introduced 'clean' organellar genomes (i.e. never exposed to a mutant background) into the resulting heterozygous F1s. The presence of one WT allele in the F1 heterozygotes should be sufficient for WT-like organelle genome maintenance since the mutant alleles of the repair genes of interest are thought to act recessively (Shedge *et al.* 2007; Cappadocia *et al.* 2010; Rowan *et al.* 2010; Zampini *et al.* 2015; Wu *et al.* 2020; García-Medel *et al.* 2021; Chevigny *et al.* 2022). The heterozygous F1s were then allowed to self-cross and we identified three homozygous mutant and three homozygous WT F2s, which were also allowed to self-cross. Families of F3 seeds were grown together to obtain sufficient leaf tissue for organelle isolation and mutation detection via Duplex Sequencing.

The only notable differences between the methods in this study compared to Wu et al. 2020 were 1) we only isolated organelles for which the protein of interest is targeted (plastid: *OSB2*, *RADA,* and *RECA1*; mitochondrial: *RADA, RECA3, and WHY2*), whereas in Wu *et al.,* (2020) we isolated both organelles regardless of targeting. 2) We adjusted our Duplex Sequencing library construction protocol to obtain larger inserts by ultrasonicating the DNA for only 60 seconds (three bouts of 20 seconds, with 15 second pauses between each) and size selecting libraries with a 2% gel on a BluePippin (Sage Science), using a specified target range of 400-700 bp. 3) We implemented a new approach to filter spurious

variant calls resulting from nuclear insertions of mtDNA and cpDNA (NUMTs and NUPTs) by comparing putative mutations directly against the *A. thaliana* nuclear genome (TAIR 10.2; Berardini *et al.* 2015) and the new assembly of the large NUMT on chromosome 2 (Fields *et al.* 2022), replacing the *k*-mer based NUMT/NUPT filtering approach described in Wu *et al.* (2020).

Generation and analysis of nanopore sequencing libraries for structural variant detection

Nanopore libraries were produced from the same DNA samples that were used for Duplex Sequencing. Sequencing libraries were created following the protocol outlined in the Oxford Nanopore Technologies Rapid Barcoding Kit 96 (SQK-RBK110-96) manual (v110 Mar 24, 2021 revision) and were sequenced on MinION flow cells (FLO-MIN106) under the control of MinKNOW software v22.08.4 or 22.08.9. Multiplexed libraries from cpDNA samples were pooled and run on a single flow cell, whereas pooled mtDNA libraries were run on two flow cells. All runs were conducted for 72 hrs with a minimum read length of 200 bp. Data were processed using the Guppy Basecalling Software v6.3.4+cfaa134.

We sequenced three mutant replicates and one matched WT control for each gene of interest. Mutant lines for the cpDNA samples included *msh1* (CS3246)*, osb2, recA1,* and *radA* (only two *radA* mutants were sequenced due to a lack of DNA in mutant replicate 2), while mutant lines for the mtDNA samples included *msh1* (CS3246)*, recA3, why2,* and *radA*. The total sequencing yield (3.72 Gb) in our initial run of 15 cpDNA samples was an order of magnitude higher than our subsequent run with the 16 mtDNA samples (0.33 Gb). To increase mtDNA coverage we re-sequenced 12 of those mtDNA samples (all but the *msh1* mutants and matched WT control) in a third run, which had a similar low yield (0.42 Gb) to the second run. In all cases, samples were run on fresh flow cells as opposed to flow cells that had been washed for a second run. Because the *msh1* and *radA* mtDNA samples produced very little data (Table S4), we used the mtDNA contamination in the *msh1* and *radA* cpDNA samples in downstream analyses of the nanopore data.

To calculate mitochondrial and plastid read depth, we aligned the nanopore reads to the organellar genomes with minimap2 (version 2.24; Li 2018) and tabulated depth at each position with bedtools (version 2.30.0; Quinlan and Hall 2010). We calculated the average depth in 1000-bp sliding windows tiling the organellar genomes and plotted depth as a normalized mutant:WT ratio.

The nanopore reads were analyzed with HiFiSr (https://github.com/zouyinstein/hifisr), a software tool developed to identify structural variants using BLASTn alignments of long reads in plant organellar genomes (Zou *et al.* 2022). Because the tool was originally developed for PacBio HiFi reads, which are more accurate than nanopore reads, we required at least two independent nanopore reads to support putative indels. In addition, we constrained our analysis to reads with only one or two BLASTn hits, disregarding the reads with three or more BLASTn hits (which may originate from reads that span two or more recombined repeats). For reads with two BLASTn hits, we compared the breakpoints of putative recombination events with the repeats in the *A. thaliana* organellar genomes, which are reported in Tables S10 (mtDNA) and S28 (cpDNA) by Zou *et al.* (2022). We calculated recombination frequencies for each repeat pair as the number of recombined reads divided by the total number of repeat-spanning reads. To compute genome-wide repeat frequencies, we restricted the analyses to repeats that showed a total of at least ten mtDNA recombination reads across all replicates. Because cpDNA recombination events were much less common, we lowered the threshold to a minimum of three recombining reads per repeat for calculating recombinaiton frequencies. All of the matched WT controls were averaged for comparisons againsnt the mutant variant frequencies because we only sequenced one WT control for each gene of interest.

RESULTS

Duplex Sequencing coverage

We generated Duplex Sequencing libraries from DNA extracted from isolated organelles to test if genes involved in recombination-suppression also impact accumulation of SNVs and

short indels in *A. thaliana* organellar genomes. Duplex Sequencing libraries were sequenced on a NovaSeq 6000 to produce between 30.6 to 139.1 million paired-end reads (2×150 nt) per library (Table S2). Processing the Duplex Sequencing libraries to collapse Illumina reads into consensus sequences and map them to organellar genomes resulted in coverage of 94.2 to 816.3× in the mitochondrial libraries (*radA, recA3,* and *why2*) and 234.2 to 1176.6× in the plastid libraries (*radA, recA1,* and *osb2*; Table S2).

Increased SNV and indel frequency in *radA*, *recA1*, and *recA3* mutants

We compared variant frequencies of each mutant to the matched WT controls (two-tailed *t*-test) and found significant increases in SNV and indel frequencies in the *radA* mutants (p-values reported in Fig. 1). We also observed significant indel and weakly significant SNV increases in the *recA3* and *recA1* mutants in the mtDNA and cpDNA, respectively. We analyzed our previously generated *recA3* mutant from Wu *et al.,* (2020), which represents an independent mutant allele of *recA3*, and similarly found significant indel and weakly significant SNV increases in mtDNA (Fig. S1). In total, we detected 204 SNVs and 123 indels in the newly generated Duplex Sequencing libraries (File S1). Dinucleotide mutations involve neighboring sites both experiencing a substitution at the same time and are increasingly being recognized as an important type of mutation (Kaplanis *et al.* 2019). We assessed whether these mutations increase in frequency in any of the analyzed mutant backgrounds but found no significant differences relative to WT controls (Wilcoxon signed rank test, $p > 0.05$, Fig. S2).

Decreased frequency of CG→TA transitions in the mtDNA of newly generated WT lines

The mutant lines assayed in both this study and in Wu *et al.* (2020) were sequenced with matched WT controls. Surprisingly, pooled WT SNV frequencies generated in the current study were lower than the pooled WT SNV frequencies from the Wu *et al.* (2020) dataset (2.8×10^{-8} vs. 1.7×10^{-7}, *t*-test, $p = 8.9\times10^{-12}$), driven by a decrease in CG→TA transitions (*t*-test, $p = 2.2\times10^{-10}$; Fig. 2, File S1). To understand if the decreased SNV rate in the newly generated WT libraries (Fig. 2) resulted from the changes we made to our library

preparation protocol, we created a Duplex Sequencing library following our new protocol using one of the original WT DNA samples from Wu *et al.,* (2020). This new library had an SNV rate of 1.57×10^{-7} which is in line with the SNV rates observed in the WT libraries from the 2020 study (Fig 2). In fact, the new SNV rate for this DNA sample was slightly higher than that of the original library (1.39×10^{-7}). Given that the newly created libraries were all size selected on a BluePippin, which involves mixing the libraries with fluorescein labeled DNA as an internal standard for gauging DNA migration speed, we re-sequenced two stored libraries from Wu *et al.,* (2020) with and without size selection on the BluePippin. The inclusion of the sample without size selection on the BluePippin served as a control for the sample processed on the BluePippin and also as an independent test to understand if changes in the sequencing platform could be responsible (all samples were sequenced on a NovaSeq 6000, but the chemistry of the flow cells has been updated). These re-sequenced libraries had SNV rates typical of the old WT libraries of 1.97×10^{-7} (size selected library) and 1.47×10^{-7} (not size selected). Again, these values were slightly higher than the SNV rates from the original round of sequencing ($1.\ 36\times10^{-7}$ and 1.39×10^{-7}, respectively). Therefore, it seems highly unlikely that the decreased SNV rate in the new WT libraries is associated with the changes we made to our library preparation protocol. Instead, these appear to be genuine differences in the DNA samples, perhaps due to unknown variation in the growth conditions or DNA extraction procedures between the two batches.

SNV frequencies are similar among different genomic regions

To gain a deeper understanding of mutational process in the organellar genomes, we next turned our attention to the distribution of SNVs, focusing primarily on the *msh1* mutants and the pooled WT libraries from the Wu *et al.* (2020) study, given the larger number of mutations in those datasets. First, we assessed if the SNVs in *msh1* mutants and pooled WT libraries from Wu *et al.* (2020) are evenly distributed between intergenic, protein-coding (CDS), intronic, rRNA, and tRNA regions (Fig. 3) and found no significant differences among genomic regions (Kruskal-Wallis test, $p > 0.05$, Table S3) except in the WT plastid comparison, which is likely not biologically meaningful, given the small number of

observed WT plastid SNVs (Fig. 2). Given that the vast majority of mtDNA SNVs in the Wu *et al.* (2020) WT dataset are CG→TA transitions, we separately tested if this class of substitutions is evenly distributed across regions and found significant differences (Kruskal-Wallis test, $p = 0.0295$), driven by a decrease in tRNA genes compared to intergenic sequences (pairwise comparisons with Wilcoxon rank sum test, $p=0.0013$). However, tRNA genes make up a small fraction of the genome and, thus, are subject to higher sampling variance, precluding any confident conclusions about whether they actually accumulate fewer CG→TA transitions than intergenic sequence.

C→T substitutions are more common on the template strand in genic regions

Next, we performed a strand asymmetry analysis to understand if the SNVs in these datasets are evenly distributed on template vs. non-template (i.e., sense or coding) strands in the CDS, intronic, rRNA, and tRNA regions of the organellar genomes. The analysis of the CG→TA transitions from the Wu *et al.* (2020) WT dataset revealed that G→A substitutions are significantly enriched on the non-template strand of the DNA (paired Wilcoxon signed-rank test; $p < 0.05$ for CDS, rRNA and tRNA genes). Conversely, C→T substitutions predominately occur on the template strand, which is read by RNA polymerases during transcription (Fig. 4). This asymmetry is most striking in rRNA and tRNA genes, where every C→T substitution occurred on the template strand (25 in rRNA and 7 in tRNA). CG→TA transitions were also asymmetrically distributed between strands in genic regions of the Wu *et al.* (2020) *msh1* mutants (Fig. 5), though only in certain regions of the mtDNA (Fig. 5 top right panel), and not in the cpDNA (Fig. 5 bottom right panel). We also investigated strand asymmetries in the AT→GC transitions of the Wu *et al.* (2020) *msh1* mutants and found a trend toward more C→T substitutions on the template strand of plastid genes (Fig. 5 left panels). We did not investigate strand asymmetries for the other substitution classes in WT or *msh1* mutants because the small number of data points precludes meaningful comparisons between strands (see Fig. 5 of Wu *et al.* 2020).

CG→TA transition frequencies vary depending on trinucleotide context

To understand how surrounding nucleotides impact SNV accumulation in plant organellar genomes, we performed a trinucleotide analysis, again focusing on CG→TA transitions in WT and both transition types in *msh1* mutants, due to a lack of data in other substitution classes. In the WT dataset (Wu *et al*. 2020), we found that CG→TA transitions are 8.4-fold more common in the mtDNA and 3.7-fold more common in the cpDNA when the C is 3′ of a pyrimidine (Fig. 6). Interestingly, this same trinucleotide context (5′ pyrimidine) is not enriched for CG→TA transitions in the *msh1* mutant data. Instead CG→TA transitions are 3.0-fold more common when the C is 5′ of a G in the *msh1* mutants (Fig. 7 right panels). Meanwhile AT→GC transitions are 1.8-fold more common when the A is 5′ of a C (Fig. 7 left panels). In all cases, these trinucleotide mutation frequencies are normalized by the total coverage of a given trinucleotide context so that the values are not inflated in trinucleotides that are relatively common in the mtDNA.

Chloroplast extractions produced an order of magnitude more nanopore sequencing data than mitochondrial extractions

We next generated long-read Oxford Nanopore libraries to gain a deeper understanding of how the genes in our panel impact plant organellar genome stability. Unexpectedly, the libraries produced from the mitochondrial isolations sequenced poorly compared to the plastid-derived libraries (see methods), so we investigated cross-organelle contamination (mtDNA molecules in the plastid-derived samples and cpDNA molecules in mitochondrially derived samples) to understand if poor mtDNA sequencing performance was inherit to the mtDNA or associated with differences in the organellar isolation methods. The level of mtDNA contamination in the plastid-derived nanopore libraries is similar to the level of contamination in the Duplex Sequencing libraries (Fig. S3). The average median read length of the mitochondrial derived nanopore libraries is about 2.5-fold higher than the average median read length of the plastid-derived libraries (2.48 kb vs. 1.08 kb, respectively). In the plastid derived nanopore libraries, the median lengths of the contaminating mtDNA reads tend to be slightly longer than the median lengths of native cpDNA reads (average median lengths of 1.17 kb vs 0.98 kb, respectively), though there is

substantial variation between samples (Fig. S4). In the mitochondrially derived libraries, the contaminating cpDNA and native mtDNA median read lengths show more correlation (average median lengths of 2.41 kb and 2.56 kb, respectively; Fig. S4).

These analyses suggest that the difference in yields for the different nanopore runs is likely related to differences in the organellar isolation methods. One unique feature of the mitochondrial isolation protocol is the use of a DNase I treatment to remove contaminating nuclear and plastid DNA molecules (Wu *et al.* 2020). It is possible that this treatment results in nicking of the mtDNA that interrupts the molecules as they are threaded through the nanopore in a single-stranded fashion. Such nicking would not be expected to disrupt Duplex Sequencing library creation since the first step of making Duplex Sequencing libraries is to break DNA into small fragments via ultrasonication. However, this explanation is somewhat inconsistent with the 2.5-fold greater median read length in the mitochondrially derived nanopore libraries. Fortunately, the contaminating mtDNA derived reads in the *msh1* and *radA* cpDNA sequenced samples provided sufficient mtDNA coverage for analyzing structural variation in the mtDNA (Table S4, Figure S3 left panel).

Repeat-mediated recombination drives distinct patterns of mtDNA instability in *msh1*, *radA*, and *recA3 mutants*

Given the known role of recombination-related genes in maintaining organellar genome copy number and structural stability (Arrieta-Montiel *et al.* 2009; Davila *et al.* 2011; Miller-Messmer *et al.* 2012; Chevigny *et al.* 2022; Zou *et al.* 2022), we analyzed the ratio of mutant coverage to WT coverage to characterize structural perturbations on a genome-wide level (Fig. 8). We see distinct variation patterns in the mtDNA coverage in *msh1, radA* and *recA3* mutants, consistent with the expected structural effects of these genes (Fig. 8) and similar to previously documented coverage patterns (Wu *et al.* 2020; Chevigny *et al.* 2022). In contrast, the *why2* coverage does not deviate from WT coverage, suggesting there is no substantial and consistent structural effect of losing *why2*. In *recA3*, the nanopore and Duplex Sequencing lines are tightly correlated, while the nanopore data tends to show

353 greater variance in the *msh1, radA*, and *why2* plots, perhaps because of the lower
354 nanopore coverage in those samples (Table S5; Figs. S6 and S67). Interestingly, *radA* and
355 *recA3* share many major coverage peaks and valleys, suggesting genome structure is
356 perturbed in similar ways in these mutants (Fig. 8, Figs S6 and S7). Compared to the
357 mitochondrial samples, the cpDNA samples display much less coverage variation (Fig. S5),
358 with a notable exception in the *recA1* nanopore data. However, inspection of the coverage
359 in the individual cpDNA replicates (Fig. S8) reveals depth irregularities in the WT control
360 compared to the other WT samples. Regardless, the *recA1* Duplex Sequencing data does
361 not show any depth variation along the cpDNA, so the nanopore result does not appear to
362 reflect a biological effect on cpDNA structure. One other intriguing pattern in the cpDNA
363 plots is an apparent correlation in peaks and valleys in *radA* and *osb2* in the Duplex
364 Sequencing data (most notable is the shared valley at 112 kb). However, inspection of the
365 individual *recA1* mutant and matched WT control replicates (Fig. S9) reveals all samples
366 have a dip at 112 kb and the dip is more pronounced in one or more of the *osb2* and *radA*
367 mutants. Given the large number of PCR cycles used to amplify the Duplex Sequencing
368 libraries (19 cycles) the unified movement of all replicates is likely explained in part by
369 amplification bias in AT or GC rich regions. Therefore, variation in amplification bias may
370 result in lower coverage of AT or GC rich regions, so these patterns are likely not biological.
371 We analyzed the nanopore reads for evidence of repeat-mediated recombination. To
372 do so, we calculated recombination frequencies for each repeat pair as the count of
373 nanopore reads that recombined at a given repeat (according the BLASTn alignments
374 generated by HiFiSr (Zou *et al.* 2022)) divided by the total number of reads that mapped to
375 the repeat. Table 1 shows the five repeats with the highest recombination frequency for
376 each mutant genotype and the matched WT controls. Fig. 9 shows examples of how the
377 long nanopore reads map to the mitochondrial genome following recombination at inverted
378 (Fig. 9A) or directed repeats (Fig. 9B and C).
379 We calculated genome-wide recombination frequencies for the mtDNA by summing
380 across repeats with at least 10 recombining reads (File S2). The threshold was lowered to
381 repeats with at least three recombining reads in the cpDNA given the smaller number of

recombining reads observed in the cpDNA (File S3). We found significant differences in the frequency of mtDNA rearrangements among the WT and mutant lines (one-way ANOVA, $p = 1.5\times10^{-8}$, Fig. 10), which were driven by increases in recombination frequency in *msh1, radA* and *recA3* compared to WT (Tukey pairwise comparison, $p = 3.0\times10^{-7}$, 2.0×10^{-7}, and 0.02, respectively). In contrast, there was no mtDNA recombination frequency difference between *why2* mutants and WT samples (Tukey pairwise comparison, $p = 0.99$). We found that different repeats apparently become active in different mutant background as evidenced by a two-way ANOVA with a significant interaction between genotype and repeat ($p < 2.0\times10^{-16}$). Because our analysis focuses on reads with two or fewer BLASTn hits, we may have underestimated global recombination frequencies, especially in mutant backgrounds, as a PacBio HiFi study found that such reads with three or more BLASTn hits (which arise when reads span two or more repats that have recombined) comprise 0.34% and 8.69% of all reads in WT and *msh1*, respectively (Zou *et al.* 2022). Consistent with previous characterization of repeat mediated recombination in plant mtDNAs (Arrieta-Montiel *et al.* 2009; Davila *et al.* 2011; Miller-Messmer *et al.* 2012; Chevigny *et al.* 2022; Zou *et al.* 2022), we found that repeat length and percent identity are also predictive of recombination frequency through a three-way ANCOVA with repeat length and percent identity as continuous variables ($p = 1.8\times10^{-12}$ and 1.4×10^{-6}, respectively) and genotype as a categorical variable ($p = 2.0\times10^{-22}$). There were no significant differences in repeat-mediated recombination between any of the cpDNA mutants (*msh1, radA, osb2,* and *recA1*) compared to the WT samples (one-way ANOVA, $p = 0.849$; Fig. 9). We identified no insertions in the HiFiSr variant calls (after requiring at least two nanopore reads to support a putative insertion) and only a single cpDNA deletion of 106 bp in *msh1* mutant replicate 2, which was supported by 18 independent nanopore reads (cpDNA position 148490-148596).

DISCUSSION

Potential causes of elevated organellar mutation rates in lines with disrupted recombination machinery

By utilizing highly accurate Duplex Sequencing for point mutation detection and long-read Oxford Nanopore sequencing for structural variant detection, we have characterized the overall organellar mutational dynamics in *A. thaliana* lines lacking genes with roles in organellar genome recombination. The increases in point mutations we observed in *radA, recA3,* and *recA1* are much smaller than the effects previously observed in *msh1* mutants (Wu *et al.* 2020) where mutants experience 6.0-fold and 116.5-fold increases in SNVs (in mtDNA and cpDNA, respectively) and 86.6-fold and 790.6-fold increases in indels (in mtDNA and cpDNA, respectively). In contrast, *radA* mutants incurred 2.6-fold and 12.6-fold more mtDNA and cpDNA SNVs (respectively) and 5.1-fold and 3.1-fold more mtDNA and cpDNA indels (respectively) than the matched WT controls. The point mutation increases in *recA3* and *recA1* were even smaller than in the *radA* mutants. One complication with directly comparing the mutant vs. WT fold changes across the newly generated mutant lines compared to those generated in Wu *et. al.,* (2020) is the decrease in WT mutation rates in the new genes (Fig. 2). Because of the shift in the baseline WT rates, the numbers cited above may actually underestimate the gap in effect size between *msh1* and the newly analyzed genes.

The point mutation increases in *msh1* mutants have clear mechanistic explanations which were first predicted based on the MSH1 mismatch recognition and GIY-YIG endonuclease domains (Christensen 2014; Wu *et al.* 2020). In contrast, given that RADA, RECA3 and RECA1 are all thought to function in the resolution of recombination intermediates, it is more difficult to explain the mechanisms responsible for increased point mutations in these lines. One possibility is that in the absence of one recombination pathway, recombining molecules are shuttled into an alternative, less faithful recombination pathway. For example, in mutant lines deficient in homologous recombination (HR), double-stranded breaks (DSBs) may be repaired via error prone non-homologous end joining (NHEJ) or MMEJ, which could drive increases in indels and SNVs (Waters *et al.* 2014; García-Medel *et al.* 2019). Evidence suggests that RADA functions as the principal branch migration factor in a primary mtDNA and cpDNA homologous recombination (HR) pathway, while RECA3 may fill the same role as RADA in a partially

redundant and less utilized mtDNA specific-HR pathway (Chevigny *et al.* 2022). Interestingly, RECA2 is thought to initiate recombination in both pathways and is essential in plants (Miller-Messmer *et al.* 2012; Chevigny *et al.* 2022). The larger SNV and indel increases in the *radA* mutants than in the *recA3* mutants may reflect the relative utilization (and importance) of these two partially redundant HR pathways (Chevigny *et al.* 2022). Similarly, previous studies have documented increased NHEJ and MMEJ in cpDNA of *recA1* mutants (Zampini *et al.* 2015), which is consistent with the significant increase in indels and marginally significant increase in SNVs reported here (Fig. 1).

Another possibility is that the rise in point mutations is an indirect effect of increased repeat-mediated recombination and its associated harm to organelle function. Increased recombination between short repeat sequences may disrupt genes, organellar genome stoichiometry, and genome organellar replication, which is recombination-dependent in plants (Shedge *et al.* 2007; Rowan *et al.* 2010; Chevigny *et al.* 2020). Plant organellar genomes encode proteins necessary for the electron transport chains of respiration and photosynthesis and disruption of these pathways can result in the excess production of DNA damaging reactive oxygen species (ROS; Liu *et al.* 2021). Although a direct link between ROS-mediated damage to DNA and mutation rates remains contentious (Kennedy *et al.* 2013; Itsara *et al.* 2014; Broz *et al.* 2021; Waneka *et al.* 2021; Sanchez-Contreras *et al.* 2021), ROS molecules have been shown to indirectly affect point mutation rates by impairing proofreading capabilities via damage to the metazoan mtDNA polymerase (Pol γ; Anderson *et al.* 2020). Impairment of organellar function is also consistent with phenotypic growth defects in *radA*, which include retarded development and distorted leaves with chlorotic sectors (Chevigny *et al.* 2022).

Potential explanations of mutational biases based on DNA strand asymmetry and flanking nucleotides

We found that SNVs in the *msh1* mutants and WT plants from Wu *et al.,* (2020) had biased distributions in terms of strand (non-template vs. template) and trinucleotide context. Such patterns are useful for understanding the underlying mechanisms driving mutation

formation (Haradhvala *et al.* 2016; Sun *et al.* 2018; Moeckel *et al.* 2023). For example, CG→TA strand asymmetries documented in diverse metazoan mtDNAs have been proposed to result from the two DNA strands experiencing unequal time in single-stranded states during mtDNA replication, since single-stranded DNA is more vulnerable to cytosine deamination (a primary driver of CG→TA transitions) (Kennedy *et al.* 2013; Itsara *et al.* 2014; Arbeithuber *et al.* 2020; Waneka *et al.* 2021; Sanchez-Contreras *et al.* 2021). In mammals, C→T substitutions are ~10-fold more common than G→A substitution on the mtDNA heavy strand (H-strand), which likely spends more time in a single-stranded state as the mtDNA is copied via a strand-asynchronous replication mechanism (Kennedy *et al.* 2013; Arbeithuber *et al.* 2020). Further, the C→T substitutions form two gradients starting at the two H-strand origins of replication, consistent with the regions closest to the origin being single stranded for longer (Sanchez-Contreras *et al.* 2021).

The substantial CG→TA strand asymmetries we observed in the mtDNA of the Wu *et al.,* (2020) WT libraries are unlikely to be explained by replication mechanisms given that plants mtDNAs lack discrete origins of replication or dedicated 'leading and lagging' strands (alternatively referred to as light and heavy strands, respectively, in some systems) and instead rely on recombination-mediated replication (Gualberto and Newton 2017; Brieba 2019; Chevigny *et al.* 2020). Instead, our strand asymmetry analysis focused on genic regions, motivated by well-established patterns of more C→T than G→A substitution on non-template strands which spend more time in exposed single-stranded during transcription (Haradhvala *et al.* 2016; Vöhringer *et al.* 2021; Moeckel *et al.* 2023). Surprisingly, we found an opposite pattern with template strands exhibiting far more C→T than G→A substitutions (Fig. 4). This effect was especially pronounced in rRNA and tRNA genes where the C→T substitutions occurred on the template strand in all 32 observed CG→TA transitions. An enrichment of C→T substitutions on template strands also occurred in the mtDNA (but not the cpDNA) of the *msh1* mutants, though there was less power for detecting statistically significant effects (Fig. 5). The overabundance of A→G compared to T→C substitutions in *msh1* mutant cpDNA template strands also occurs in the opposite direction of predicted effects given that the non-template strand is again

498 expected to experience increased adenine deamination (which leads to A→G
499 substitutions; Mugal *et al.* 2009; Sanchez-Contreras *et al.* 2021).
500 Enrichment of C→T and A→G substitutions on template strands is puzzling, and to
501 our knowledge there are no other instances where this widespread transcriptional
502 asymmetry has been reversed (Mugal *et al.* 2009; Moeckel *et al.* 2023). Reversals in strand
503 asymmetries have been reported in metazoan mitochondrial genomes, but in these cases
504 the asymmetries are replication based, and the reversals are proceeded by an inversion of
505 the origin of replication, effectively switching the leading and lagging strands (Wei *et al.*
506 2010). It is notable that the WT CG→TA asymmetries are most pronounced in the rRNA and
507 tRNA genes (Fig. 4), which are likely more highly expressed than the protein coding genes.
508 Increases in transcription have been shown to drive genomic instability in the *A. thaliana*
509 cpDNA due to the increased formation of R-loops (RNA/DNA hybrids formed by
510 displacement of the other DNA strand), which stall replication forks and lead to DSBs
511 (Pérez Di Giorgio *et al.* 2019). It is possible that increased mtDNA expression also leads to
512 the formation of R-loops and DSBs which may then be repaired through error prone NHEJ
513 and MMEJ. However, it is not clear how this would drive strand asymmetric mutation.
514 Further, such a mechanism is not consistent with the relatively even distribution of SNVs
515 across intergenic vs. transcribed regions of the genome (Fig. 3). The magnitude of the
516 CG→TA asymmetries is decreased in the *msh1* mutants (roughly 2-fold averaging across all
517 genic sequences) compared to in the WT controls (roughly 6-fold). This shift may reflect a
518 larger proportional contribution of mutations from simple DNA polymerase
519 misincorporation errors (which are not expected to be strand-biased) in the absence of
520 MSH1 activity.
521 The CG→TA transitions in the WT lines and both transitions in the *msh1* mutants
522 were also impacted by the identity of neighboring nucleotides (Figs. 6 and 7). Trinucleotide
523 effects have previously been implicated to bias mutation distribution in the *A. thaliana*
524 nuclear genome (Lu *et al.* 2021) as well as in the mtDNAs of various metazoans (Itsara *et al.*
525 2014; Arbeithuber *et al.* 2020; Waneka *et al.* 2021; Sanchez-Contreras *et al.* 2021). It is
526 noteworthy that the specific trinucleotides associated with CG→TA transitions differ

between WT and *msh1* mutants. The 5′ YCN signature (where Y is any pyrimidine and N is any nucleotide) in the WT lines is similar to that induced by APOBEC3-mediated cytosine deamination in human cell lines (Carpenter *et al.* 2023), though plants lack APOBEC enzymes so the relevance of this shared pattern is unclear. Meanwhile, the 5′ NCG signature in the *msh1* mutants is consistent with spontaneous water mediated cytosine deamination (Carpenter *et al.* 2023).

Patterns of repeat-mediated recombination differs among mutant lines

The repeat mediated mtDNA recombination activity we documented in the *msh1*, *radA* and *recA3* mutants is consistent with the previously documented recombination increases of these mutant backgrounds (Shedge *et al.* 2007; Arrieta-Montiel *et al.* 2009; Rowan *et al.* 2010; Davila *et al.* 2011; Miller-Messmer *et al.* 2012; Zampini *et al.* 2015; Wu *et al.* 2020; Chevigny *et al.* 2022; Zou *et al.* 2022). The absence of an effect in the *why2* mutants is interesting given that *why2* is the most abundant protein in mitochondrial nucleoids (Fuchs *et al.* 2020) and plants lacking *why2* display aberrant mitochondrial morphology (Golin *et al.* 2020; Negroni *et al.* 2024). On the other hand, this result is consistent with a previous study that showed *why2* mutants become more recombinationally active than WT under increased genotoxic stress (ciprofloxacin treatment) but showed no recombinational difference from WT under 'normal' growth conditions (Cappadocia *et al.* 2010; Negroni *et al.* 2024).

Though *msh1*, *radA* and *reca3* are all required for the suppression of repeat-mediated recombination in mtDNA, these proteins likely function either in independent HR pathways (*radA, recA3*) or in different ways (*msh1*). As, noted, RECA3 is thought to facilitate branch migration in an HR pathway that may be relatively minor compared to the one in which RADA functions (Chevigny *et al.* 2022). Previous studies of *recA3/msh1* and *recA3/radA* double mutants have shown the double mutants are more recombinationally active than *recA3* single mutants (Shedge *et al.* 2007), supporting the hypothesis that *RECA3*-mediated HR is at least partially independent of *RADA*-mediated HR (Miller-Messmer *et al.* 2012; Chevigny *et al.* 2022). This model is supported by the greater increase

in global recombination frequency in *radA* compared to *recA3* (Fig. 10). We might also expect different repeats to become active in *recA3* compared to *radA* mutants. However, as seen in Table1, there is substantial overlap in the repeats with increased recombination frequencies in these mutants, though the extremely high recombination frequency at repeat L in *radA* is one major difference. Meanwhile, MSH1 has been proposed to suppress non-allelic recombination by recognizing and rejecting mismatches in the invading strand during heteroduplex formation (Christensen 2018; Broz *et al.* 2022), which could be a shared feature in both *RADA* and *RECA3* dependent HR pathways. Supporting this idea, there is an increased number of repeats that become active in *msh1* mutants compared to *radA* and *recA3* mutants. Specifically, there are 12 repeat pairs with a recombination frequency greater than 0.1 in *msh1* mutants but only four and nine repeat pairs that meet this threshold in *recA3* and *radA* mutants, respectively (File S2).

Given that recombination is activated differently between the mutants (Fig. 8), the high degree of repeatability between replicates is fascinating (Figs. S5, S6, S7, S8). These repeatable patterns rely on consistent activation of distinct repeat pairs and/or consistent maintenance/replication of certain recombination products. Understanding why different repeats become active and how these patterns relate to the increase in point mutations reported here remains an important unanswered question in the field of plant organellar genome maintenance.

DATA AVAILABILITY

The Duplex Sequencing and Oxford Nanopore reads were deposited to the NCBI Sequence Read Archive (SRA) under BioProject PRJNA1113549.

FUNDING

This work was supported by the National Institutes of Health (NIGMS R35GM148134).

582 **TABLES**

583 **Table 1. Repeat-specific recombination frequencies at the five most**
584 **recombinationally active mtDNA repeats for each genotype**

Genotype	Recombined reads	Total repeat spanning reads	Recomb. freq.	Repeat name	Repeat pair coordinates	Percent ID	Length
msh1	49	178	**0.284**	**B**	41464-41999, 32196-321431	99.81	537
msh1	51	199	**0.268**	**A***	19682-20237, 34620-346763	99.82	556
msh1	40	157	**0.256**	G	30938-31272, 27139-271061	99.40	335
msh1	36	171	**0.242**	**MMJS**	134427-135193, 257452-258143	88.66	767
msh1	48	203	**0.222**	**D**	6118-6569, 84540-84089	97.79	452
radA	94	125	**0.692**	**L***	270775-271023, 331877-332125	100	249
radA	135	262	**0.476**	**A***	19682-20237, 34620-346763	99.82	556
radA	201	529	**0.4**	**EE***	65547-65673, 73611-73737	99.21	127
radA	124	284	**0.357**	**F***	206095-206444, 246766-247115	100	350
radA	43	258	**0.144**	X	288315-288518, 306969-307174	97.57	206
recA3	198	907	**0.227**	**L***	270775-271023, 331877-332125	100	249
recA3	210	1384	**0.168**	**EE***	65547-65673, 73611-73737	99.21	127
recA3	159	1019	**0.149**	**F***	206095-206444, 246766-247115	100	350
recA3	88	770	**0.116**	**A***	19682-20237, 34620-346763	99.82	556
recA3	67	1111	0.06	I*	30442-30722, 255122-254842	99.64	281
why2	1	274	0.042	unnamed	239143-239268, 26378-263905	91.27	126
why2	5	256	0.007	**A***	19682-20237, 34620-346763	99.82	556
why2	5	272	0.007	**F***	206095-206444, 246766-247115	100	350

why2	5	260	0.007	**L***	270775-271023, 331877-332125	100	249
why2	3	219	0.005	**D**	6118-6569, 84540-84089	97.79	452
WT	23	902	0.093	**A***	19682-20237, 34620-346763	99.82	556
WT	10	858	0.057	**L***	270775-271023, 331877-332125	100	249
WT	13	931	0.055	**B**	41464-41999, 32196-321431	99.81	537
WT	6	1050	0.041	C	36362-36824, 14440-143947	99.57	463
WT	11	933	0.04	**MMJS**	134427-135193, 257452-258143	88.66	767

Listed are the five most active repeats for each genotype, ordered by the recombination frequency within each genotype. Repeat names were sourced from Table S11 of Zou *et al.,* 2022. For the *msh1* mtDNA analysis, we relied exclusively the plastid-derived *msh1* samples, and for the *radA* mtDNA analysis, we used a combination of the low coverage *radA* mitochondrial samples and the plastid *radA* samples (see main text). For the WT comparison, we took the average across the single matched WT libraries that were sequenced with each mutant line, including *msh1* and *radA* WT plastid samples (Table S4). The repeats that are also plotted in Figure 8 are denoted with an asterisk. Repeats which make are among the top five most active repeats in more than one genotype are bolded. Repeat-specific recombination frequencies that exceed 0.1 are shown in bold, and note that none of the WT or *why2* repeat specific recombination frequencies meet this threshold.

FIGURES

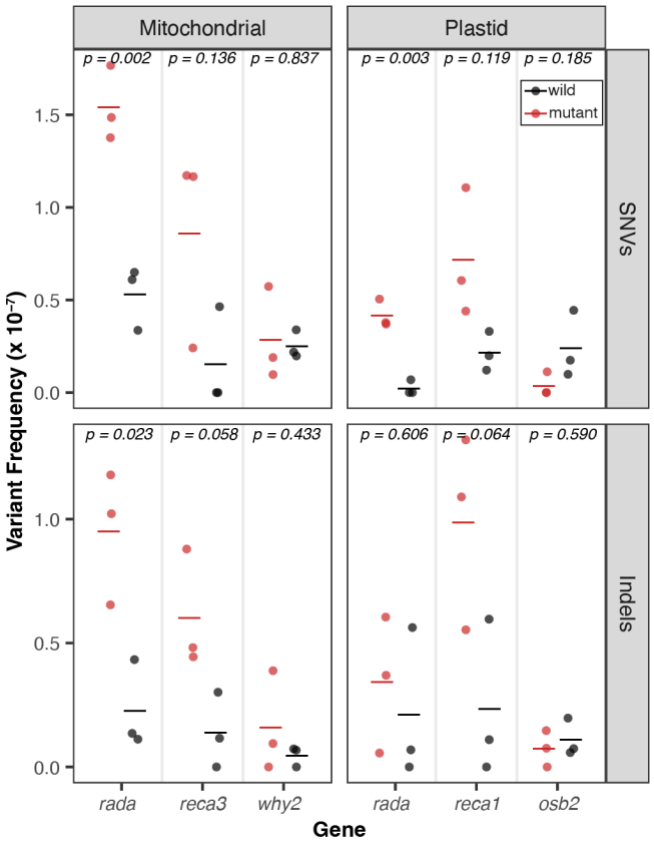

Figure 1. *De novo* point mutations measured with Duplex Sequencing. For each gene of interest (x-axis), mutant lines are plotted in red, and matched WT controls are plotted in black. The individual biological replicates are plotted as circles and group averages are plotted as dashes. Panels separate the data by genome; left column: Mitochondria and right column: Plastid, and by point mutation type; top row: SNVs and bottom row: indels. Variant frequencies (y-axis) were calculated as the total number of SNVs/total Duplex Sequencing coverage. P-values show the result of a two-tailed *t*-test comparing WT vs mutant mutation frequencies for each gene of interest.

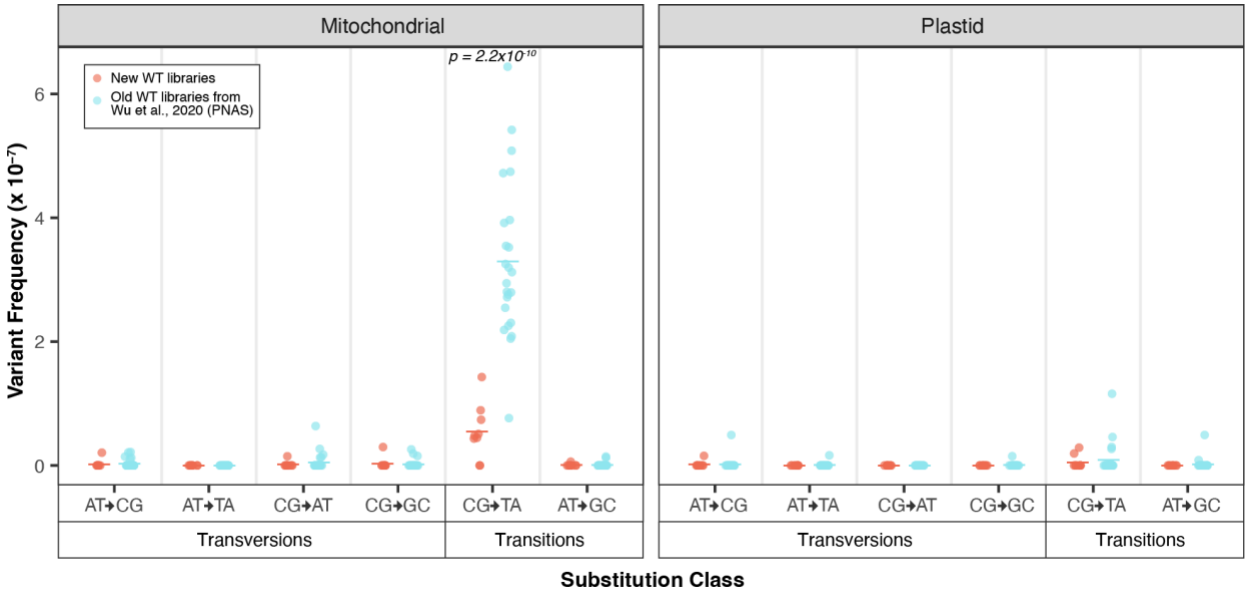

606 Figure 2. Comparison of the mutational spectrum of pooled WT controls from the current
607 study (orange) vs. the WT controls from Wu *et al.* 2020 (blue). The two panels show the
608 mitochondrial and plastid data and the x-axis separates substitutions type by transversions
609 vs. transitions and further by the six types of substitutions. Individual biological replicates
610 are plotted as circles while group averages are plotted as dashes. Only CG→TA transitions
611 showed a significant increase in the old data set (two-tailed t-test; $p=2.2\times10^{10}$).

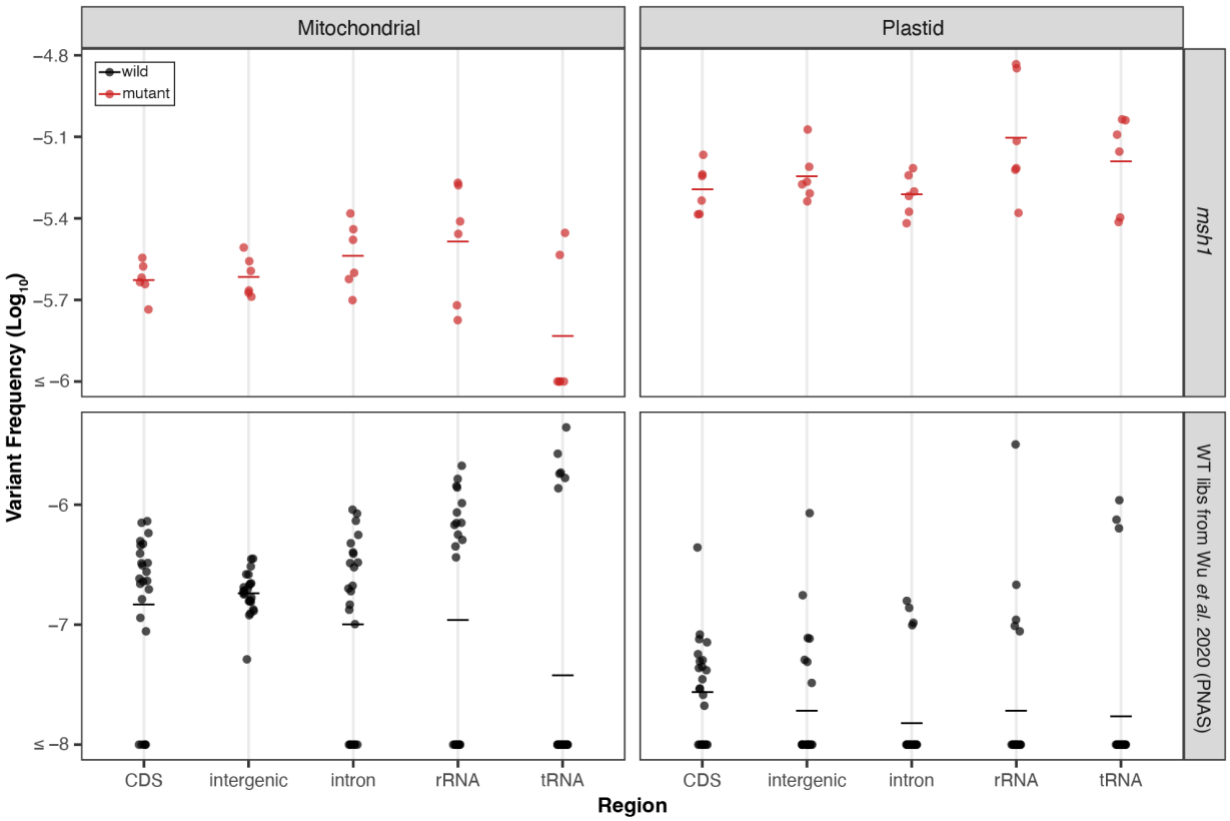

612 Figure 3. Distribution of WT (black) and *msh1* (red) SNVs (from Wu et al., 2020) across
613 genomic region. The individual biological replicates are plotted as circles and group
614 averages are plotted as dashes. Panels separate the data by genome; left column:
615 Mitochondria and right column: Plastid, and by genotype with *msh1* mutants on top and
616 WT on the bottom. Note the difference in y-axis scale for *msh1* mutants and WT. For each
617 of the four panels, we performed a Kruskal-Wallis test and found no significant difference
618 between genomic regions except the WT plastid panel ($p = 0.022$) where comparisons
619 between regions are likely not biologically meaningful given the low number of WT plastid
620 mutations. Note that for this and subsequent analyses of the *msh1* Duplex Sequencing
621 data, we pooled the two null *msh1* alleles to increase statistical power.

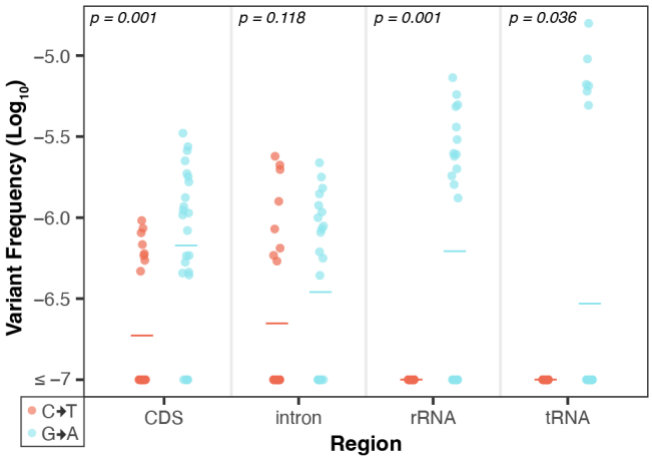

Figure 4. Strand asymmetry analysis of CG→TA transitions in the WT mtDNA Duplex Sequencing data from Wu *et al.* (2020). Shown are the log-transformed SNV frequencies (y-axis) of C→T (red) vs. G→A (blue) mutations on the non-template strand of all genes, separated by genomic region (x-axis). The individual biological replicates are plotted as circles and group averages are plotted as dashes. P-values show the result of paired Wilcoxon tests comparing the complementary substitution classes in each genomic region. In all but intronic regions, G→A substitutions are significantly higher on the non-template strand (conversely, C→T substitutions are significantly higher on the template strand). Strikingly, in all of the observed CG>TA transitions in the rRNA and tRNA genes the C→T substitution occurred on the template strand (i.e., all the G→A substitutions occurred on the non-template stand) .

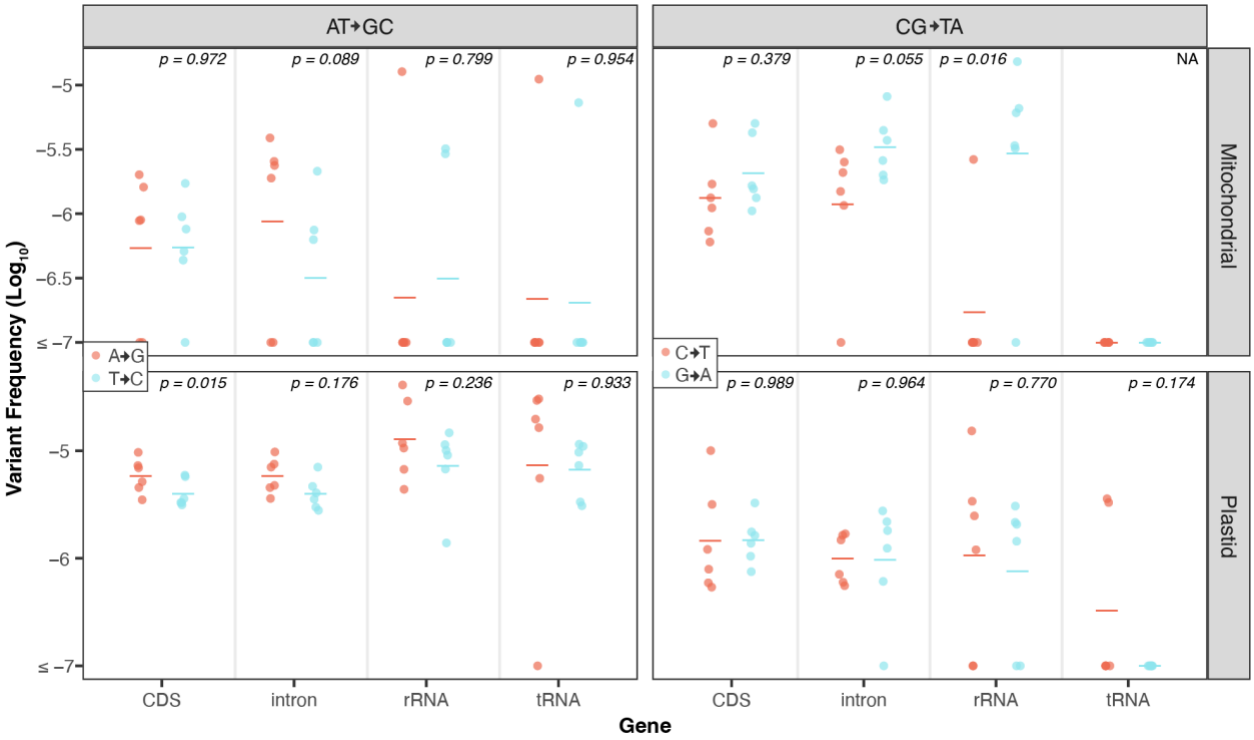

633 Figure 5. Strand asymmetry analysis of CG→TA and AT→GC transitions in the *msh1* Duplex
634 Sequencing data from Wu *et al.* (2020). Shown are the log-transformed SNV frequencies (y-
635 axis) of mutations on the non-template strands of all genes with complementary
636 substitution types designated by color (see figure legends for colors of specific substitution
637 types). The individual biological replicates are plotted as circles, and group averages are
638 plotted as dashes. The panels divide the data by transition type, with AT→GC transitions on
639 the left and CG→TA transitions shown on the right, and by genome, with mitochondrial
640 data on the top and plastid data on the bottom. Transversions were not analyzed because
641 there were relatively few observed mutations of this type in the *msh1* duplex data. P-values
642 show the result of paired *t*-tests comparing the complementary substitution classes in
643 each genomic region.

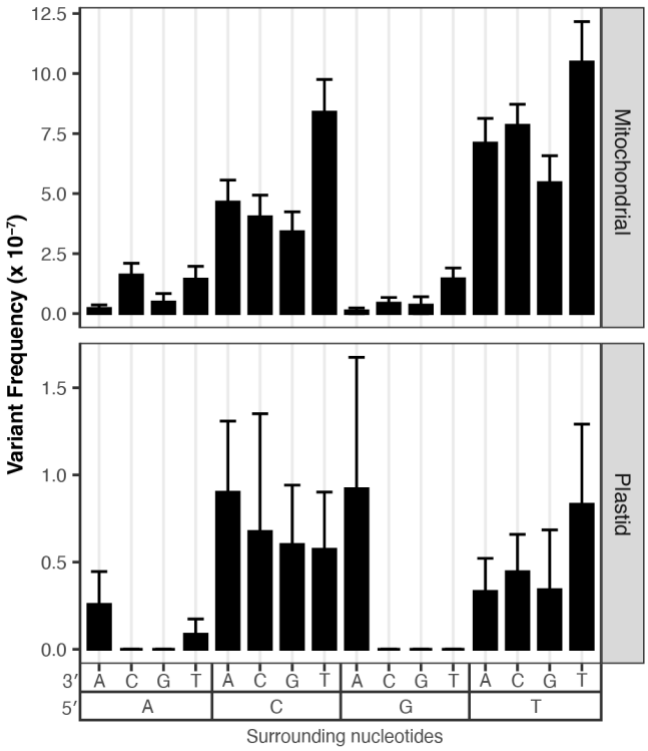

644 Figure 6. Analysis of surrounding nucleotides on C→T transition frequencies in the WT
645 Duplex Sequencing data from Wu *et al.* (2020). The panels divide the data based on
646 genome with mitochondrial data on the top and plastid data on the bottom, note the
647 difference in the y-axis scale, as CG>TA were less frequent in the plastid. The x-axis
648 captures the trinucleotide context with downstream nucleotides displayed next to the 3′
649 and upstream nucleotides display next to the 5′. The data suggest that trinucleotide
650 contexts with upstream pyrimidines (5′ CCN 3′ and 5′ TCN 3′, where N is any nucleotide)
651 have increased frequencies of C>T substitutions.

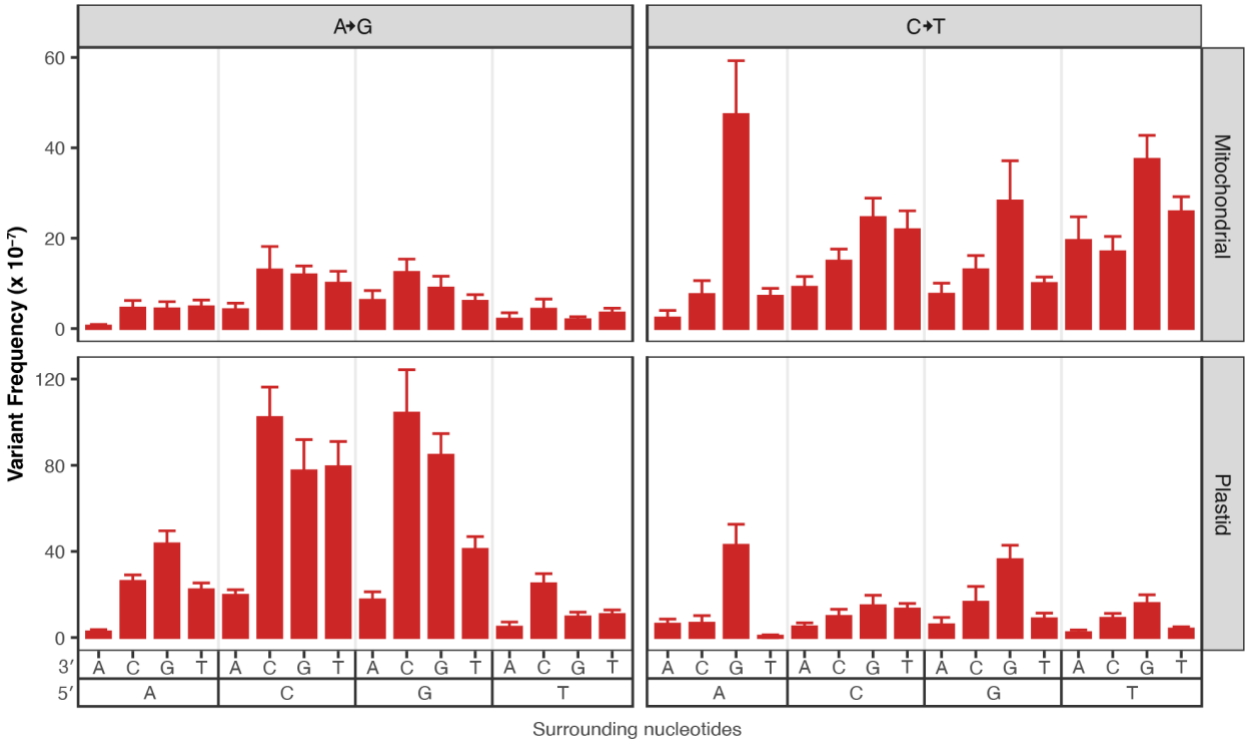

652 Figure 7. Analysis of surrounding nucleotides on A→G and C→T transition frequencies in
653 the *msh1* Duplex Sequencing data from Wu *et al.* (2020). The panels divide the data based
654 on substitution type (A→G substitutions on the left and C→T substitutions on the right) and
655 by genome (mitochondrial data on the top and plastid data on the bottom). The x-axis
656 captures the trinucleotide context with downstream nucleotides displayed next to the 3′
657 and upstream nucleotides display next to the 5′. The A→G data suggest that trinucleotide
658 contexts with downstream Cs (5′ NAC 3′) have increased frequencies of A→G
659 substitutions. The C→T data suggest that trinucleotide contexts with downstream Gs (5′
660 NCG 3′) have increased frequencies of C→T substitutions.

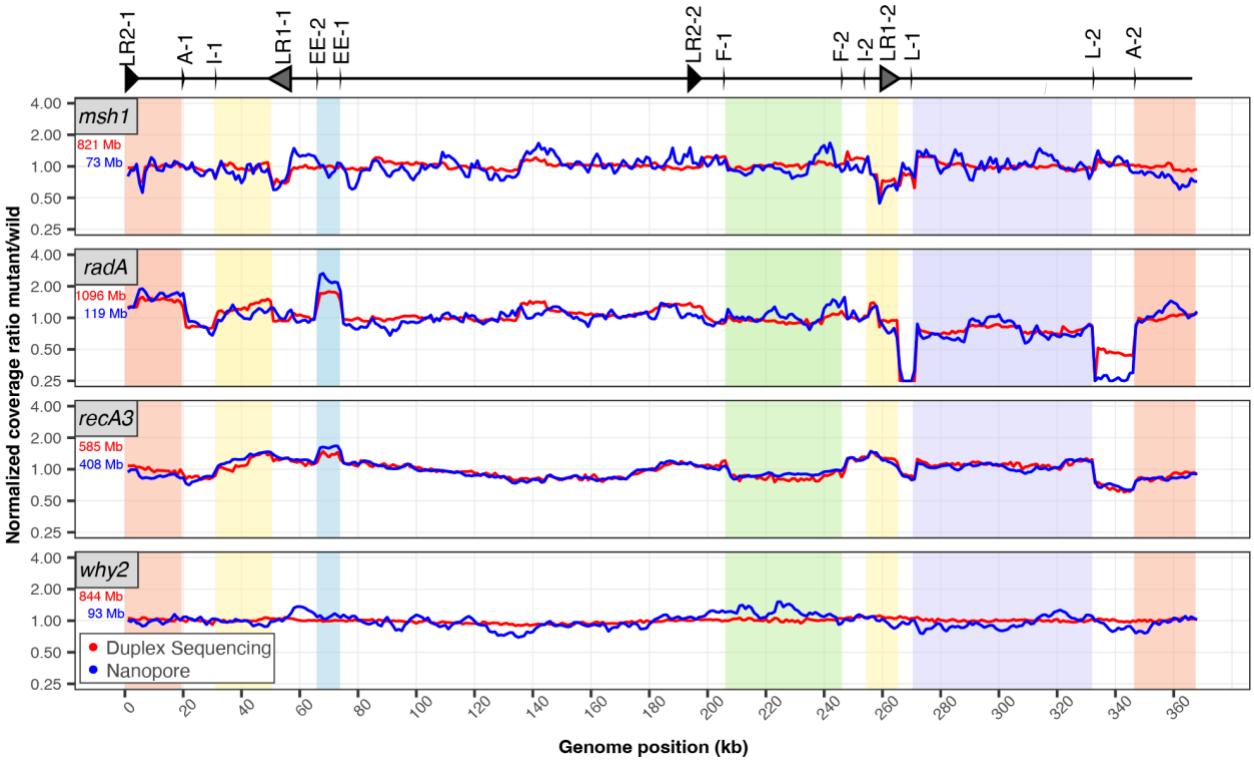

Figure 8. Normalized coverage of mitochondria genomes in mutant lines of interest . Coverage of each Duplex Sequencing (red) or nanopore (blue) library was calculated in 1000-bp windows. Mutant coverage was pooled and divided by WT coverage and the resulting ratios were normalized to 1 for plotting. The total amount of sequencing data used to generate each plot is shown in the top left corner of each panel (red=Duplex Sequencing and blue=nanopore) and is included to highlight the instances where disagreement between the Duplex Sequencing and nanopore lines may be explained by increased variance in the nanopore sample due to lower mtDNA coverage. Repeats that are likely important for driving coverage variation across the mtDNA are plotted above (also see, Table 1) according to Figure 6 of Chevigny *et al.* 2022. Regions with altered stoichiometry and flanked by repeats are shown as colored blocks, as in Figure 6 of Chevigny *et al.* 2022.

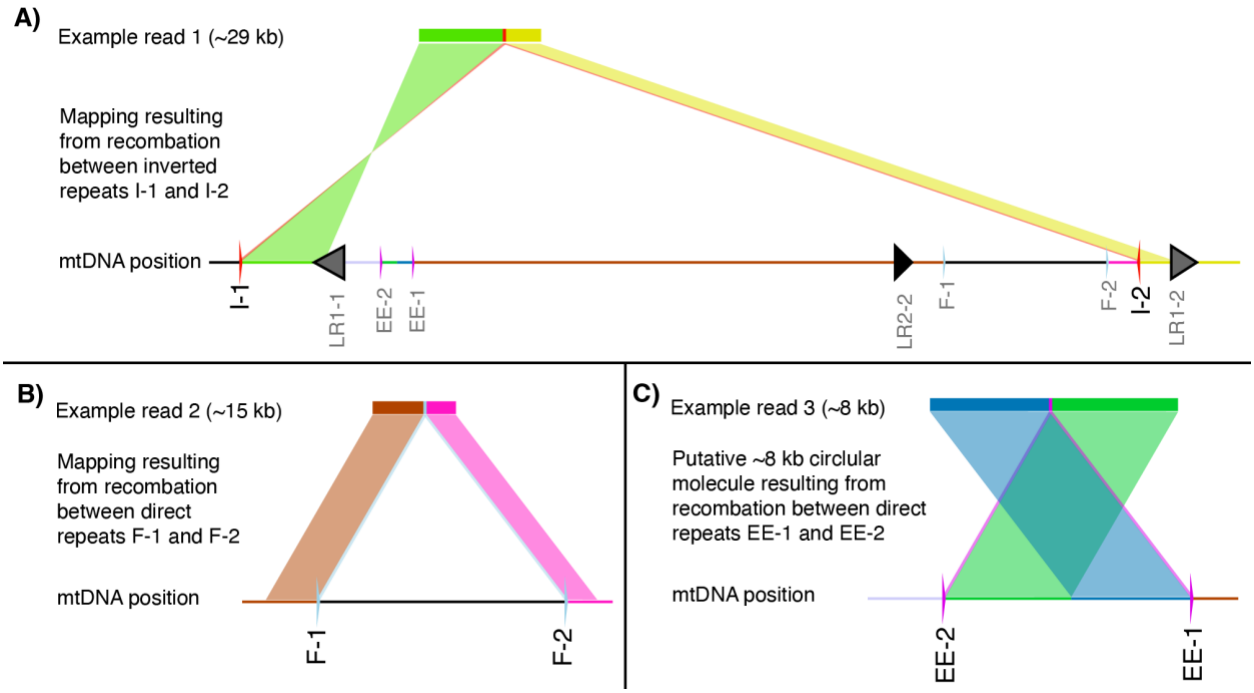

Figure 9. Examples of 3 nanopore reads from *radA* mitochondrial replicate 1 that capture repeat-mediated recombination. Nanopore reads that derive from recombination between inverted repeats map with two hits, one in the forward orientation and the other in the reverse orientation, both flanked by the sequence of a repeat, as shown in A where the 29-kb read is flanked by repeats I-1 and I-2. Recombination between direct repeats results in two hits in the same orientation with a deletion of the intervening sequence (B). The alternative product of recombination between direct repeats is the production of a small circular molecule. We identified a number of putative circular molecules or tandem duplications mediated by recombination between repeats EE-1 and EE-2, which map with two hits in the same orientation, but with a section of the end of the read mapping in front of the end of the read (C).

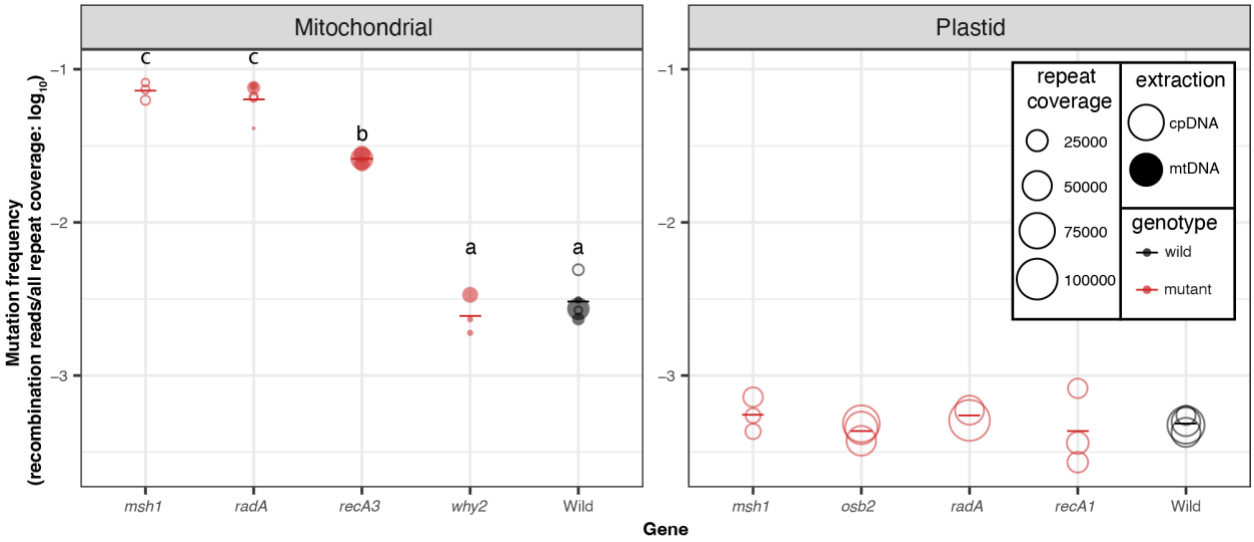

672 Figure 10. Frequency of repeat-mediated structural variants in the nanopore data. The
673 individual biological replicates are plotted as circles with the size of the circle scaled by the
674 number of repeats that are covered in the nanopore alignments. Closed circles are the
675 libraries from mitochondrial extractions, while the open circles are libraries from the
676 plastid extractions. In some cases, cpDNA extractions were used to harvest contaminating
677 mtDNA-mapping reads because of low yield from direct sequencing of the mtDNA
678 extractions. Group averages are plotted as dashes. Mutants are plotted in red, while WT
679 samples are plotted in black. Letters represent statistically significant groupings according
680 to Tukey pairwise comparisons on a one-way ANOVA ($p<0.001$). There were no differences
681 among plastid genotypes.

682 **SUPPLEMENTAL FIGURES**

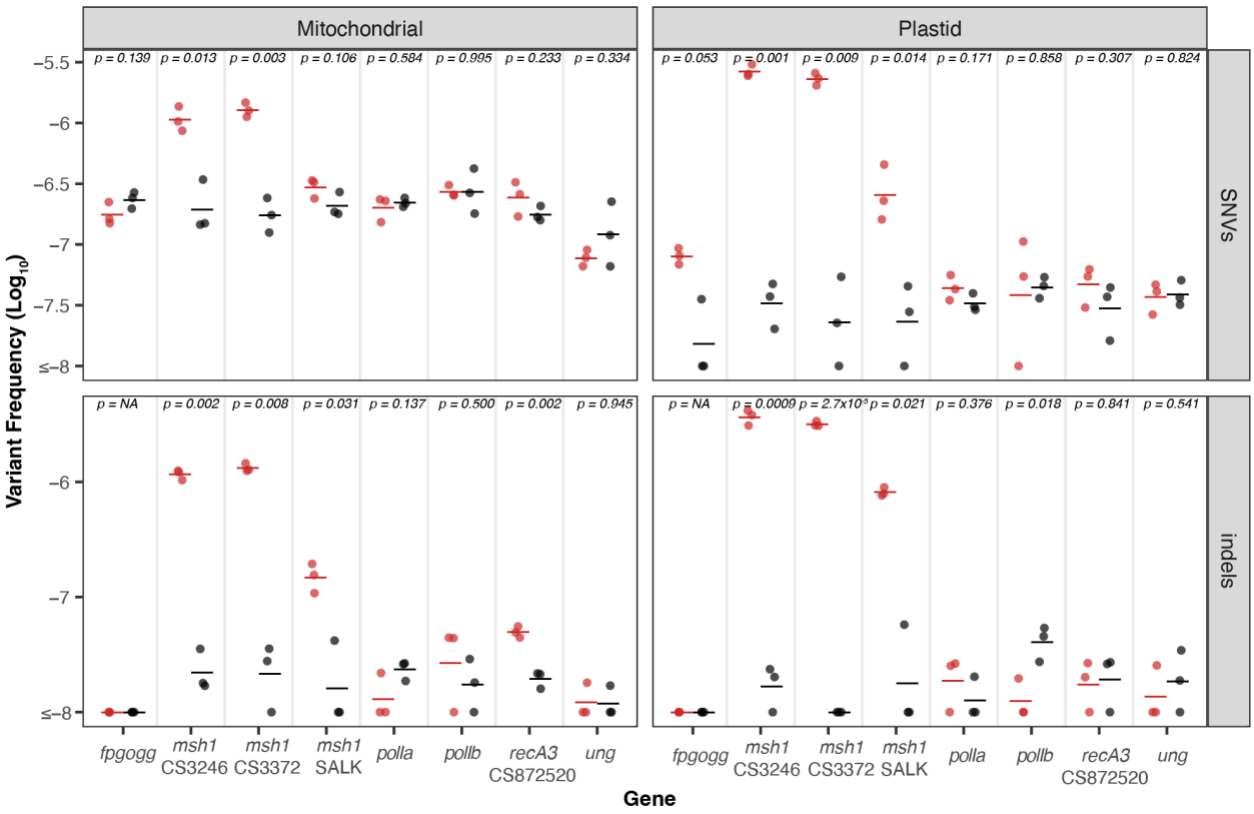

683 Figure S1. *De novo* point mutations measured with Duplex Sequencing from data generated
684 in Wu *et al.* 2020. For each gene of interest (x-axis) mutant lines are plotted in red and
685 matched WT controls are plotted in black. The individual biological replicates are plotted
686 as circles, and group averages are plotted as dashes. Panels separate the data by genome
687 (left column: Mitochondria and right column: Plastid) and by point mutation type (top row:
688 SNVs and bottom row: indels). The y-axis shows the log-transformed SNV frequencies
689 (total SNVs/total DCS coverage). P-values show the result of a two-tailed *t*-test comparing
690 WT vs mutant mutation frequencies for each gene of interest. We found significant
691 increases in SNV and indel frequencies in the *msh1* CS3246 and *msh1* CS3372 mutants
692 (both genomes) but the *msh1* SALK046763 mutant, which is not a complete knockout of
693 the *msh1* gene (Wu *et al.,* 2020) had weaker effects. In addition, we note that this *recA3*
694 null allele is different from the *recA3* null allele that was reported in the new dataset, but
695 both yielded similar results: significant indel and weakly significant SNV increases in
696 mtDNA of the *recA3* mutant. Also note the marginally significant difference in *fpg/ogg*

697 plastid SNVs is explained by just 5 SNVs in mutants and a single SNV in the WT controls,

698 which we do not consider to be a biologically meaningful difference.

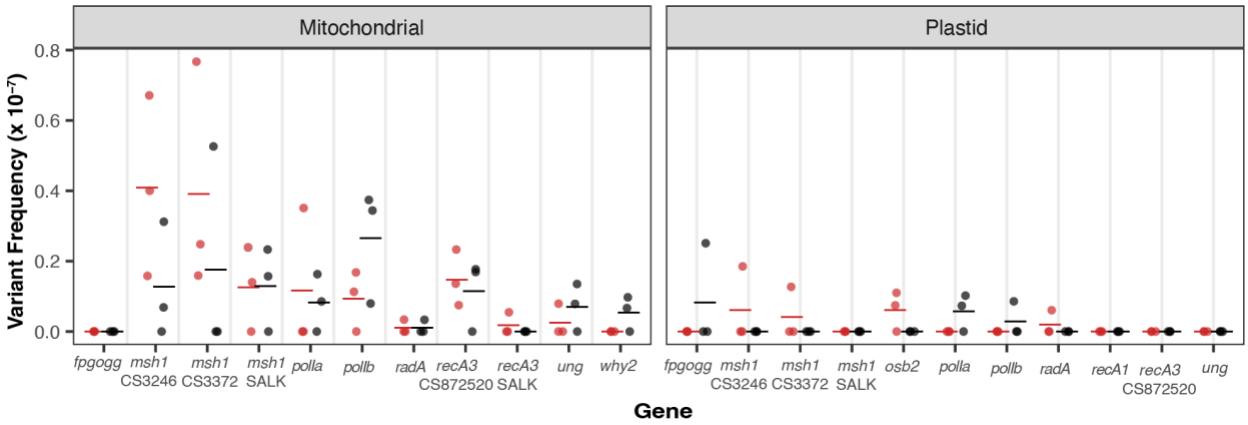

699 Figure S2. Dinucleotide mutations measured with Duplex Sequencing. For each gene of
700 interest (x axis) mutant lines are plotted in red, and matched WT controls are plotted in
701 black. The individual biological replicates are plotted as circles, and group averages are
702 plotted as dashes. Panels divide the data by mitochondrial and plastid. We performed
703 Wilcoxon rank sum tests to look for differences between mutant and matched WT controls
704 and all p-values were > 0.05. Note that *recA3* CS872520 dataset was generated in Wu *et al.*
705 (2020), and the *recA3* SALK 146388 dataset was generated in this study.

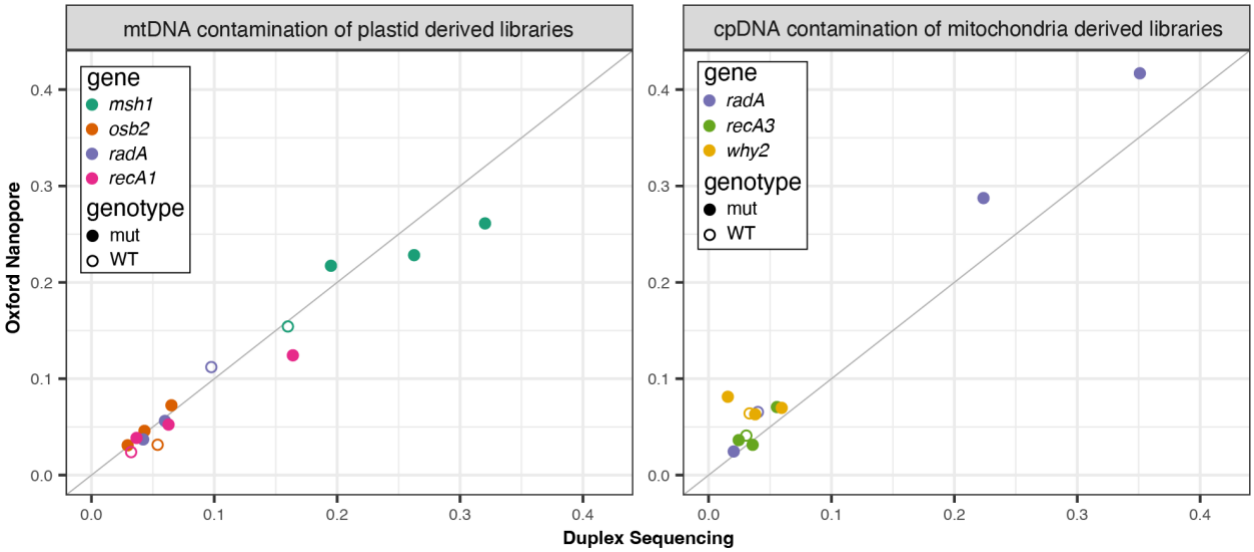

706 Figure S3. Correlation of cross-organelle contamination in Oxford Nanopore and Duplex
707 Sequencing libraries. Contamination is calculated as the number of contaminating reads in
708 the read alignments divided by the total number of organellar alignments. The different
709 mutant lines are colored according to the figure legend with mutant replicates plotted
710 using closed circles and matched WT controls plotted with open circles. The 1:1 diagonal
711 line is shown in gray. Though the level of contamination varies between different DNA
712 samples (for example mtDNA contamination is higher in the plastid derived *msh1* libraries)
713 the contamination levels are generally similar irrespective of sequencing technique. Note,
714 For the *msh1* mtDNA analysis, we relied exclusively the plastid-derived *msh1* samples,
715 and for the *radA* mtDNA analysis, we used a combination of the low coverage *radA*
716 mitochondrial samples and the plastid *radA* samples (see main text).

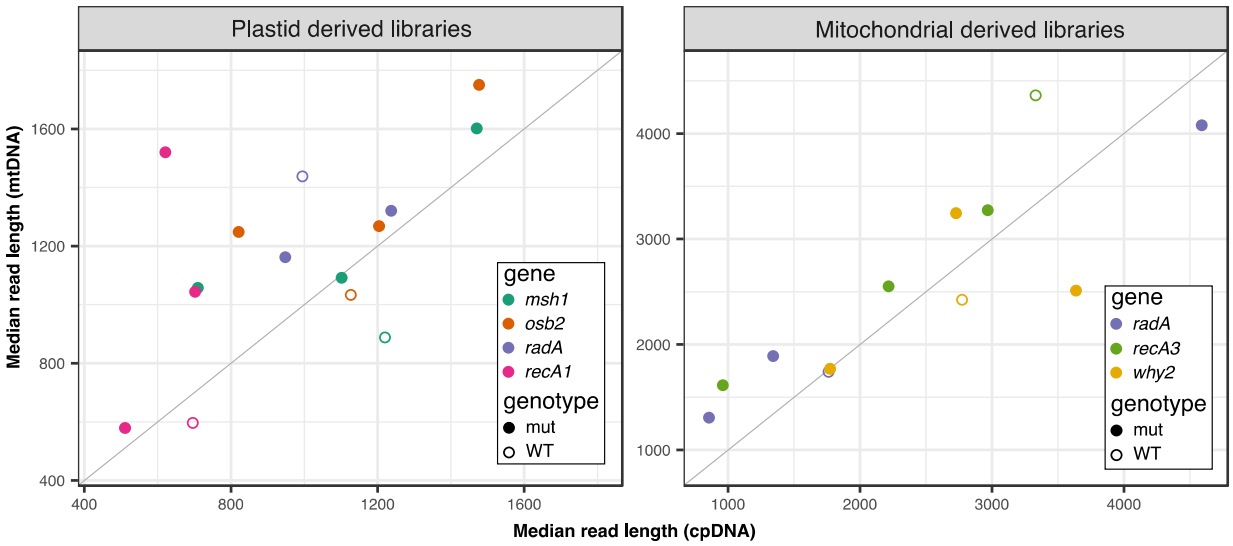

717 Figure S4. Median read length cross-organelle contaminating and native reads in the
718 plastid and mitochondrial derived nanopore libraries. The different mutant lines are
719 colored according to the figure legend with mutant replicates plotted using closed circles
720 and matched WT controls plotted with open circles. The 1:1 diagonal line is show in gray.
721 Note, For the *msh1* mtDNA analysis, we relied exclusively the plastid-derived *msh1*
722 samples, and for the *radA* mtDNA analysis, we used a combination of the low coverage
723 *radA* mitochondrial samples and the plastid *radA* samples (see main text).

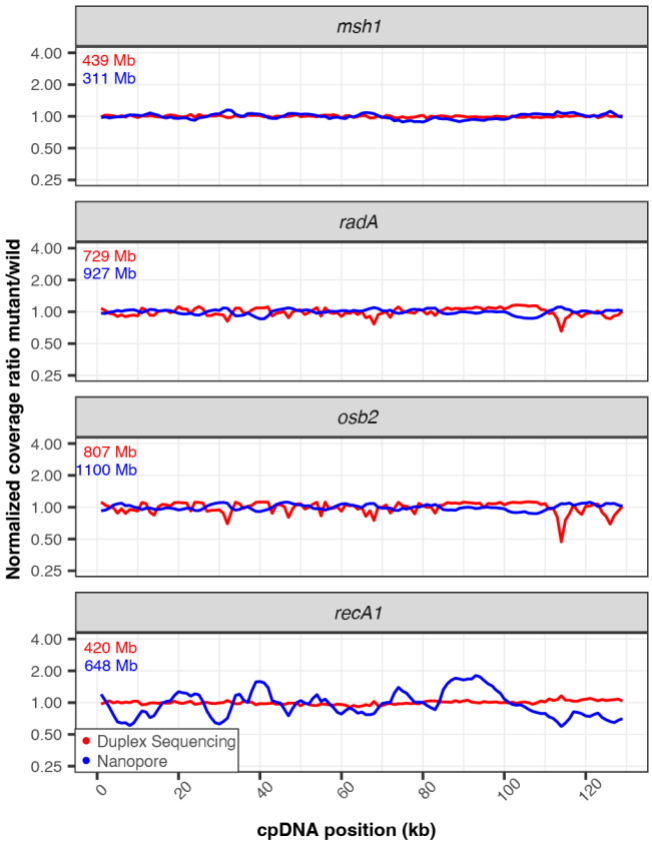

724 Figure S5. Normalized coverage of plastid genomes in mutant lines of interest . Coverage of
725 each Duplex Sequencing (red) or nanopore (blue) library was calculated in 1000-bp
726 windows. Mutant coverage was pooled and divided by WT coverage and the resulting ratios
727 were normalized to 1 for plotting. The total amount of sequencing data used to generate
728 each plot is shown in the top left corner of each panel (red=Duplex Sequencing and
729 blue=nanopore) and is included to highlight the instances where disagreement between
730 the Duplex Sequencing and nanopore lines may be explained by increased variance in the
731 nanopore sample due to lower mtDNA coverage. To see the coverage of the individual
732 replicates see Fig S8 and S9.

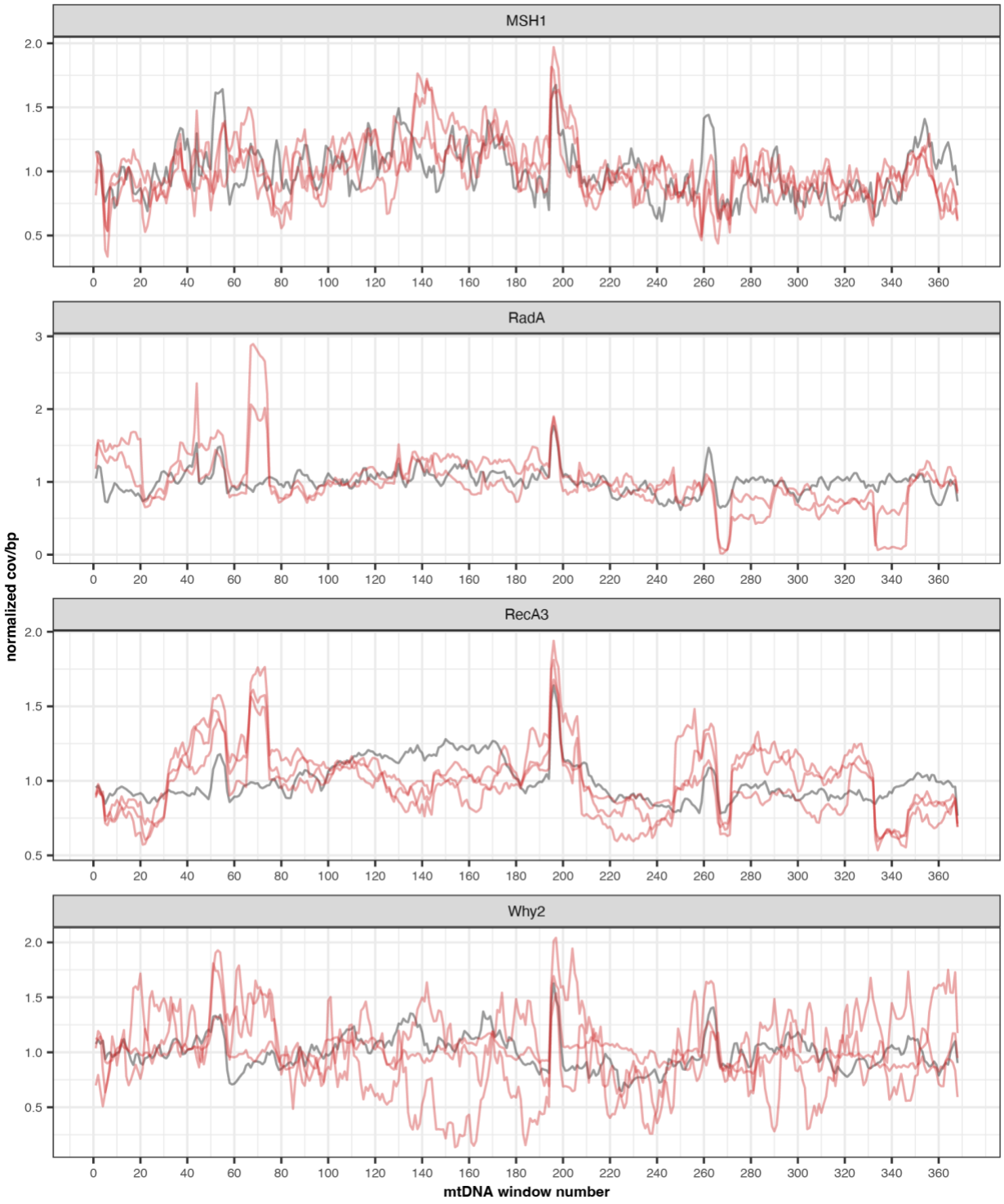

733 Figure S6. Normalized coverage of the individual nanopore mtDNA replicates (used to
734 generate Fig. 8). The red and black lines show the normalized coverage of the mutant
735 replicates and the matched WT control, respectively. Note that variation in the *why2*

736 mutants is likely due to extremely low coverage in these samples (average coverage per bp
737 of 157.3, 6.5 and 7.0 in mutant replicates 1, 2 and 3, respectively).

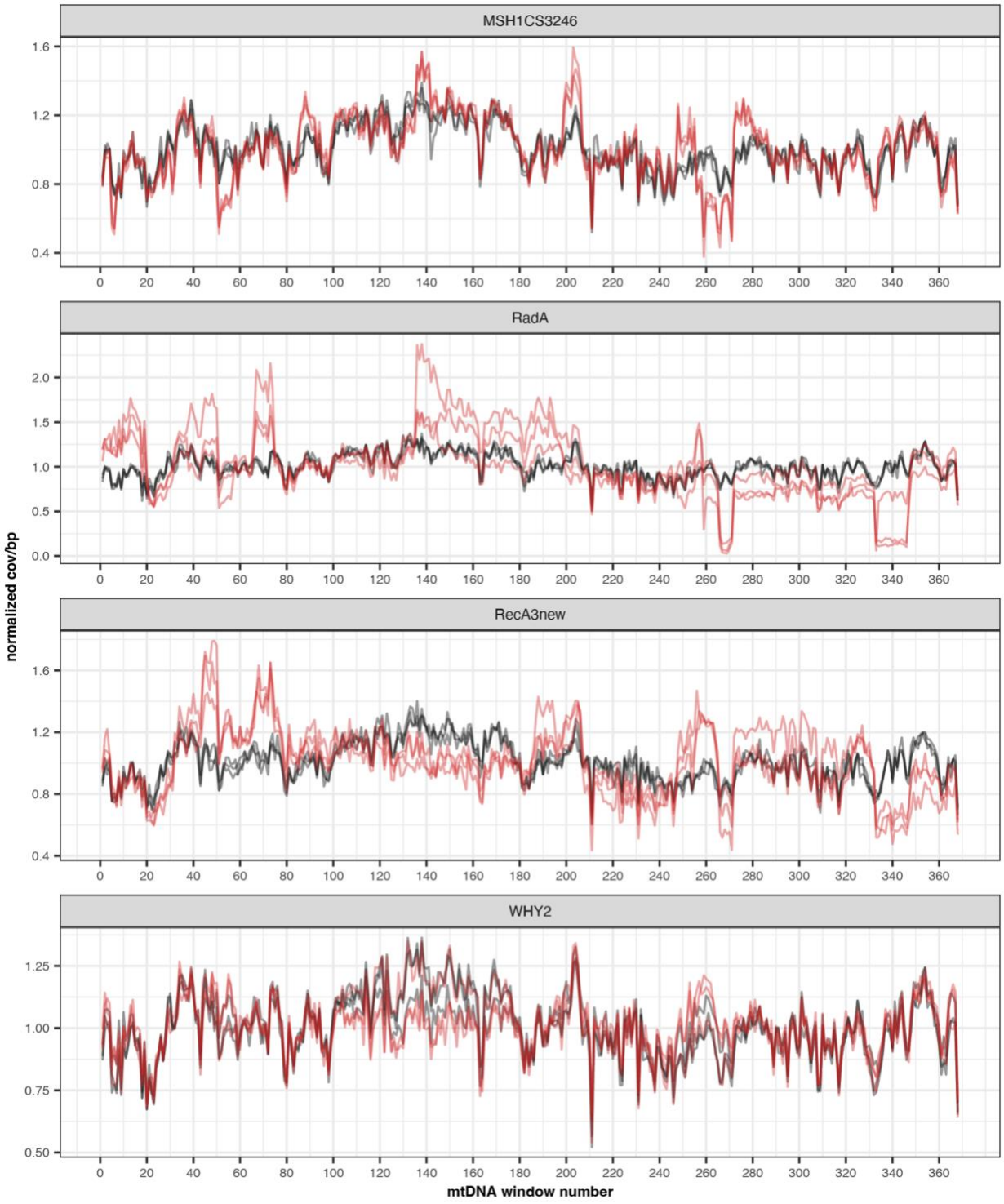

738 Figure S7. Depth of coverage of the individual Duplex Sequencing mtDNA replicates (used
739 to generate Fig. 8). The red and black lines show the normalized coverage of the mutant
740 replicates and the matched WT control, respectively.

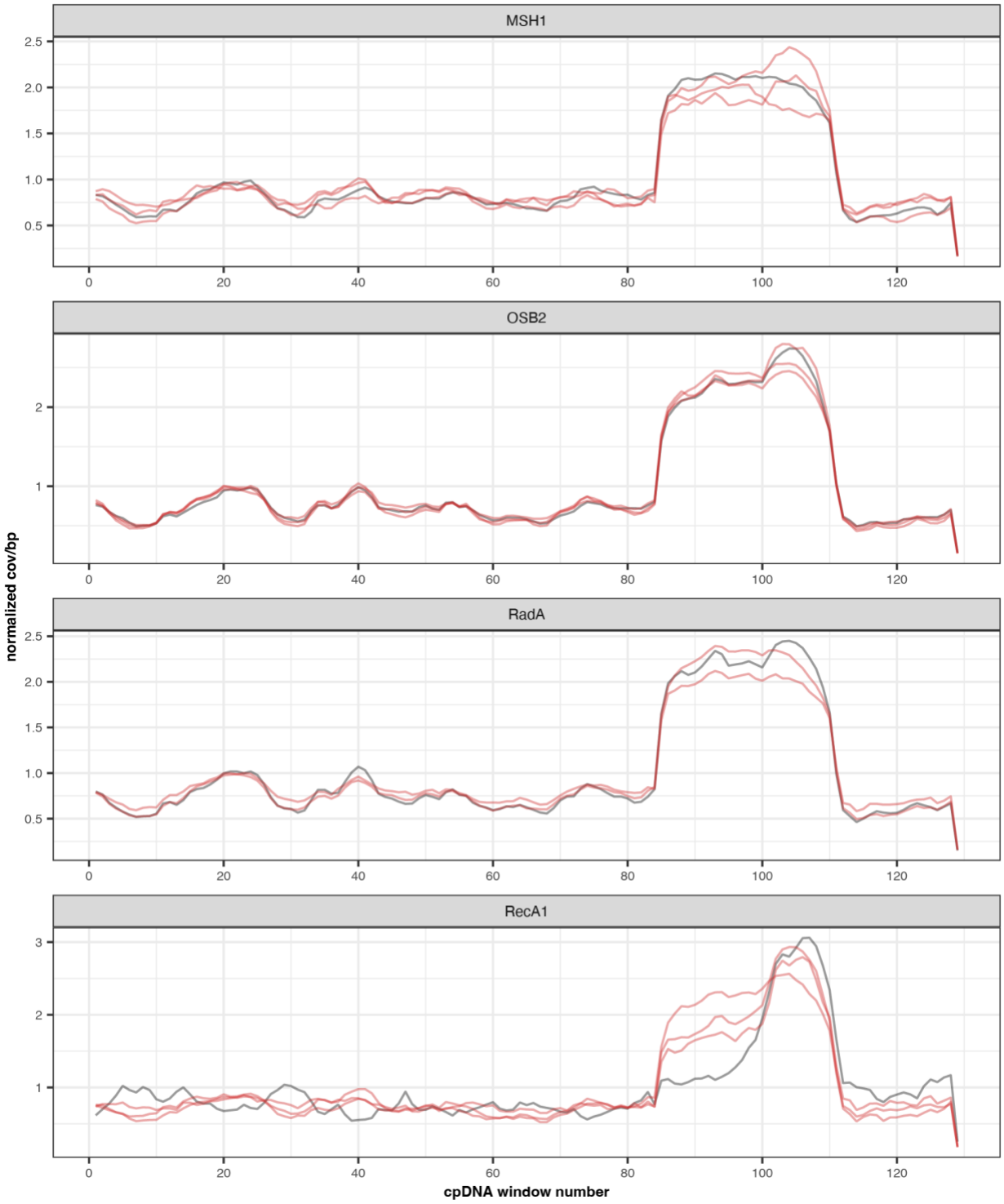

741 Figure S8. Normalized of coverage of the individual nanopore cpDNA replicates (used to
742 generate Fig. 8). The red and black lines show the normalized coverage of the mutant
743 replicates and the matched WT control, respectively. Note that the spike in coverage at
744 ~84-112 kb results from the large inverted repeat, since these reads were mapped

745 noncompetitively with minimap2 (see methods). The second copy of the inverted repeat

746 was omitted for plotting.

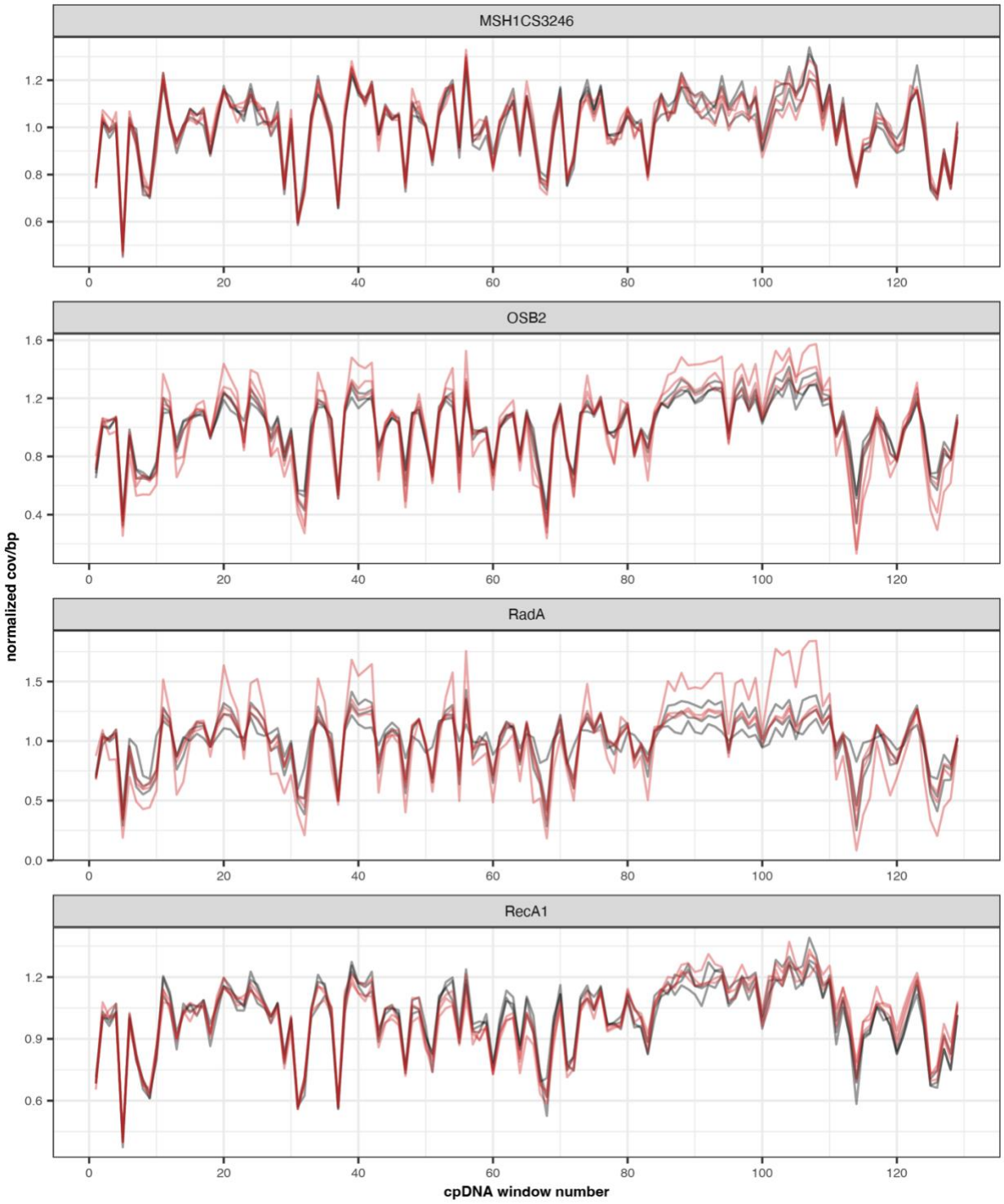

747 Figure S9. Normalized coverage of the individual Duplex Sequencing cpDNA replicates
748 (used to generate Fig. 8). The red and black lines show the normalized coverage of the
749 mutant replicates and the matched WT control, respectively. Note these reads were

750 mapped to a full length cpDNA but the second large inverted repeat was omitted for

751 plotting.

SUPPLEMENTAL TABLES

Table S1. Mutant lines used in this study and primers to verify plant genotype

Gene	Salk line (all from ABRC)	Locus	Forward Primer Wild	Forward Primer Mutant (LBb1.3)	Reverse Primer Wild and Mutant
radA	SALK_097880	AT5G50340	TTTCACTTATCGAGCCAGAGC	ATTTTGCCGATTTCGGAAC	ATGCCATAATGCTTTTTGCTG
recA1	SALK_072979	AT1G79050	TAGGGTGAGATTGGAATGCAG	ATTTTGCCGATTTCGGAAC	AAGAGCTGCTGCTCATCAAAG
recA3	SALK_146388	AT3G10140	CGTTTGGTCAGTTGAAGCTTC	ATTTTGCCGATTTCGGAAC	CTCCACAAGTCACTTCTTCGG
osb2	SALK_061852	AT4G20010	AGCGTGAAAGGTGAGACGTT	ATTTTGCCGATTTCGGAAC	GGGAAATAACAGTACCAGCCC
why2	SALK_118900	AT1G71260	CAGGAAGTCACTGTCAGTTAAGC	ATTTTGCCGATTTCGGAAC	ACCCATGATTTAGAAGTCTTAGAGAGG

Table S2. Duplex read-pairs and organellar genome coverage

Sample	Count of read-pairs (2x150)	Organellar coverage per bp
mitochondrial_rada_mut_1	75863350	297.9
mitochondrial_rada_mut_2	64771627	281.8
mitochondrial_rada_mut_3	139195192	803.4
mitochondrial_rada_wild_1	70847671	127.8
mitochondrial_rada_wild_2	61998713	246.9
mitochondrial_rada_wild_3	127161861	816.4
mitochondrial_reca3_mut_1	43472074	94.2
mitochondrial_reca3_mut_2	44312097	229.3
mitochondrial_reca3_mut_3	59128403	497.3
mitochondrial_reca3_wild_1	62354817	238.2
mitochondrial_reca3_wild_2	54311915	183.2
mitochondrial_reca3_wild_3	40734051	144.8
mitochondrial_why2_mut_1	63375069	338.0
mitochondrial_why2_mut_2	76906783	284.9
mitochondrial_why2_mut_3	76221972	292.6
mitochondrial_why2_wild_1	68231709	279.8
mitochondrial_why2_wild_2	81396138	379.9
mitochondrial_why2_wild_3	86880259	408.4
plastid_osb2_mut_1	47505179	1176.6
plastid_osb2_mut_2	54307516	870.8
plastid_osb2_mut_3	59415250	898.6
plastid_osb2_wild_1	59542949	1132.8
plastid_osb2_wild_2	69408084	889.7
plastid_osb2_wild_3	67727784	668.6
plastid_rada_mut_1	76116128	1174.4
plastid_rada_mut_2	68615282	871.7

plastid_rada_mut_3	45985626	1068.7
plastid_rada_wild_1	53480887	234.2
plastid_rada_wild_2	46684396	954.5
plastid_rada_wild_3	46190084	776.4
plastid_reca1_mut_1	66804365	543.7
plastid_reca1_mut_2	38396319	594.8
plastid_reca1_mut_3	30645358	299.3
plastid_reca1_wild_1	37377457	598.2
plastid_reca1_wild_2	32420159	543.5
plastid_reca1_wild_3	33351491	331.1

Table S3. Results from Kruskal-Wallis test comparing SNV frequencies among genomic regions in WT and *msh1* mutant data from Wu *et al.,* (2020)

Sample	**Kruskal-Wallis chi-squared value**	**p-value**
msh1 mitochondria	6.03	0.19
msh1 plastid	5.47	0.24
WT mitochondria	6.66	0.15
WT plastid	11.35	0.02

758 **Table S4.** Oxford Nanopore sequencing yields for each of the three runs

Sample	Sequencing run	Read count	Long reads count (>500bp)	Total yield (Mb)
plastid_recA1_wild_1	1	224238	131719	412.21
plastid_recA1_mut_1	1	82051	39041	121.45
plastid_recA1_mut_2	1	74341	32851	130.77
plastid_recA1_mut_3	1	72833	41137	167.30
plastid_radA_wild_1	1	127499	85335	307.34
plastid_radA_mut_1	1	111390	72395	297.02
plastid_radA_mut_3	1	186393	119090	540.66
plastid_osb2_wild_3	1	101793	66081	239.62
plastid_osb2_mut_1	1	143806	92534	407.94
plastid_osb2_mut_2	1	103151	74649	349.70
plastid_osb2_mut_3	1	109492	63761	260.72
plastid_msh1_wild_3	1	45501	29533	126.16
plastid_msh1_mut_1	1	36518	24441	111.72
plastid_msh1_mut_2	1	46533	26330	97.91
plastid_msh1_mut_3	1	47757	32369	153.13
mitochondrial_recA3_wild_1	2	8481	6019	56.73
mitochondrial_recA3_mut_1	2	1442	813	8.70
mitochondrial_recA3_mut_2	2	20256	14861	101.19
mitochondrial_recA3_mut_3	2	13261	8069	52.79
mitochondrial_radA_wild_3	2	2119	766	4.64
mitochondrial_radA_mut_1	2	13790	6079	22.39
mitochondrial_radA_mut_2	2	3675	154	0.90
mitochondrial_radA_mut_3	2	1384	681	6.32
mitochondrial_why2_wild_1	2	4720	2629	20.01

mitochondrial_why2_mut_1	2	9965	6992	50.01
mitochondrial_why2_mut_2	2	1112	411	3.34
mitochondrial_why2_mut_3	2	1279	287	2.78
mitochondrial_MSH1_wild_1	2	931	95	0.52
mitochondrial_MSH1_mut_1	2	959	151	0.64
mitochondrial_MSH1_mut_2	2	925	50	0.42
mitochondrial_MSH1_mut_3	2	471	34	0.22
mitochondrial_recA3_wild_1	3	16270	12616	120.48
mitochondrial_recA3_mut_1	3	1684	1028	11.65
mitochondrial_recA3_mut_2	3	13791	10705	97.58
mitochondrial_recA3_mut_3	3	13488	9944	82.53
mitochondrial_radA_wild_3	3	869	650	3.98
mitochondrial_radA_mut_1	3	18460	13217	53.96
mitochondrial_radA_mut_2	3	393	44	0.19
mitochondrial_radA_mut_3	3	1017	500	5.02
mitochondrial_why2_wild_1	3	3596	2496	18.99
mitochondrial_why2_mut_1	3	6147	3618	26.85
mitochondrial_why2_mut_2	3	1507	85	0.62
mitochondrial_why2_mut_3	3	508	92	0.77

Note that, for the *radA* mtDNA analysis, we averaged structural variant frequencies and coverages across the mitochondrially and plastid-derived samples, while for *msh1,* we relied entirely on the plastid-derived samples and did not investigate the mitochondrially derived samples, which had extremely low yield.

759 **Table S5.** Sequencing depth per bp (calculated with bedtools depth) of samples in Fig 8.

Sample	Sequencing protocol	Mutant (total cov/bp)	WT (total cov/bp)
radA_mito	nanopore	222.9	101.6
recA3_mito	nanopore	736.4	372.1
why2_mito	nanopore	170.9	82.5
msh1_mito	nanopore	161.9	36.9
radA_mito	duplex	1600.2	1377.4
recA3_mito	duplex	941.4	647.8
why2_mito	duplex	1058.7	1235.2
msh1_mito	duplex	1020.9	1209.6
msh1_plastid	nanopore	1650.1	762.0
osb2_plastid	nanopore	6862.2	1663.7
radA_plastid	nanopore	5514.3	1668.5
recA1_plastid	nanopore	2422.6	2603.1
msh1_plastid	duplex	1754.4	1645.3
osb2_plastid	duplex	3244.9	3009.4
radA_plastid	duplex	3444.6	2205.6
recA1_plastid	duplex	1606.6	1650.2

760

APPENDIX FOR SUPPLEMENTARY FILES

FileS1_mutation_counts: Coverages, mutation counts, and variant frequencies from the Duplex Sequencing analysis of data generated in this study and in Wu *et al.,* 2020.

FileS2_repeat_recomb_freq_mito: Counts of recombined reads and total repeat spanning reads used to calculate repeat specific recombination frequencies. We focused our mitochondrial analysis on repeats which has at least 10 recombined reads (across all replicates)**.**

FileS3_repeat_recomb_freq_plastid: Counts of recombined reads and total repeat spanning reads used to calculate repeat specific recombination frequencies. We focused our plastid analysis on repeats which has at least 3 recombined reads (across all replicates)**.**

REFERENCES

Abdelnoor R. V., R. Yule, A. Elo, A. C. Christensen, G. Meyer-Gauen, *et al.*, 2003 Substoichiometric shifting in the plant mitochondrial genome is influenced by a gene homologous to MutS. Proc. Natl. Acad. Sci. U. S. A. 100: 5968–5973.

Abdelnoor R. V., A. C. Christensen, S. Mohammed, B. Munoz-Castillo, H. Moriyama, *et al.*, 2006 Mitochondrial genome dynamics in plants and animals: convergent gene fusions of a MutS homologue. J. Mol. Evol. 63: 165–173.

Alverson A. J., S. Zhuo, D. W. Rice, D. B. Sloan, and J. D. Palmer, 2011 The mitochondrial genome of the legume Vigna radiata and the analysis of recombination across short mitochondrial repeats. PLoS One 6: e16404.

Anderson A. P., X. Luo, W. Russell, and Y. W. Yin, 2020 Oxidative damage diminishes mitochondrial DNA polymerase replication fidelity. Nucleic Acids Res. 48: 817–829.

Arbeithuber B., J. Hester, M. A. Cremona, N. Stoler, A. Zaidi, *et al.*, 2020 Age-related accumulation of de novo mitochondrial mutations in mammalian oocytes and somatic tissues. PLoS Biol. 18: e3000745.

Arrieta-Montiel M. P., V. Shedge, J. Davila, A. C. Christensen, and S. A. Mackenzie, 2009 Diversity of the Arabidopsis mitochondrial genome occurs via nuclear-controlled recombination activity. Genetics 183: 1261–1268.

Ayala-García V. M., N. Baruch-Torres, P. L. García-Medel, and L. G. Brieba, 2018 Plant organellar DNA polymerases paralogs exhibit dissimilar nucleotide incorporation fidelity. FEBS J. 285: 4005–4018.

Berardini T. Z., L. Reiser, D. Li, Y. Mezheritsky, R. Muller, *et al.*, 2015 The Arabidopsis information resource: Making and mining the “gold standard” annotated reference plant genome. Genesis 53: 474–485.

Boore J. L., 1999 Animal mitochondrial genomes. Nucleic Acids Res. 27: 1767–1780.

Brieba L. G., 2019 Structure-Function Analysis Reveals the Singularity of Plant Mitochondrial DNA Replication Components: A Mosaic and Redundant System. Plants 8. https://doi.org/10.3390/plants8120533

Broz A. K., G. Waneka, Z. Wu, M. Fernandes Gyorfy, and D. B. Sloan, 2021 Detecting de novo mitochondrial mutations in angiosperms with highly divergent evolutionary rates. Genetics 218. https://doi.org/10.1093/genetics/iyab039

Broz A. K., A. Keene, M. F. Gyorfy, M. Hodous, I. G. Johnston, *et al.*, 2022 Sorting of mitochondrial and plastid heteroplasmy in *Arabidopsis* is extremely rapid and depends on MSH1 activity. Proceedings of the National Academy of Sciences 119: e2206973119.

Cappadocia L., A. Maréchal, J.-S. Parent, E. Lepage, J. Sygusch, *et al.*, 2010 Crystal structures of DNA-Whirly complexes and their role in Arabidopsis organelle genome repair. Plant Cell 22: 1849–1867.

Carpenter M. A., N. A. Temiz, M. A. Ibrahim, M. C. Jarvis, M. R. Brown, *et al.*, 2023 Mutational impact of APOBEC3A and APOBEC3B in a human cell line and comparisons to breast cancer. PLoS Genet. 19: e1011043.

Chen C., Q. Li, R. Fu, J. Wang, C. Xiong, *et al.*, 2019 Characterization of the mitochondrial genome of the pathogenic fungus Scytalidium auriculariicola (Leotiomycetes) and insights into its phylogenetics. Sci. Rep. 9: 17447.

Chevigny N., D. Schatz-Daas, F. Lotfi, and J. M. Gualberto, 2020 DNA Repair and the Stability of the Plant Mitochondrial Genome. Int. J. Mol. Sci. 21. https://doi.org/10.3390/ijms21010328

Chevigny N., F. Weber-Lotfi, A. Le Blevenec, C. Nadiras, A. Fertet, *et al.*, 2022 RADA-dependent branch migration has a predominant role in plant mitochondria and its defect leads to mtDNA instability and cell cycle arrest. PLoS Genet. 18: e1010202.

825 Christensen A. C., 2014 Genes and Junk in Plant Mitochondria—Repair Mechanisms and
826 Selection. Genome Biol. Evol. 6: 1448–1453.

827 Christensen A. C., 2018 Mitochondrial DNA Repair and Genome Evolution. Annual Plant
828 Reviews online 11–32.

829 Davila J. I., M. P. Arrieta-Montiel, Y. Wamboldt, J. Cao, J. Hagmann, *et al.*, 2011 Double-
830 strand break repair processes drive evolution of the mitochondrial genome in
831 Arabidopsis. BMC Biol. 9: 64.

832 Drouin G., H. Daoud, and J. Xia, 2008 Relative rates of synonymous substitutions in the
833 mitochondrial, chloroplast and nuclear genomes of seed plants. Mol. Phylogenet.
834 Evol. 49: 827–831.

835 Fields P. D., G. Waneka, M. Naish, M. C. Schatz, I. R. Henderson, *et al.*, 2022 Complete
836 Sequence of a 641-kb Insertion of Mitochondrial DNA in the Arabidopsis thaliana
837 Nuclear Genome. Genome Biol. Evol. 14. https://doi.org/10.1093/gbe/evac059

838 Fuchs P., N. Rugen, C. Carrie, M. Elsässer, I. Finkemeier, *et al.*, 2020 Single organelle
839 function and organization as estimated from Arabidopsis mitochondrial proteomics.
840 Plant J. 101: 420–441.

841 García-Medel P. L., N. Baruch-Torres, A. Peralta-Castro, C. H. Trasviña-Arenas, A. Torres-
842 Larios, *et al.*, 2019 Plant organellar DNA polymerases repair double-stranded breaks
843 by microhomology-mediated end-joining. Nucleic Acids Res. 47: 3028–3044.

844 García-Medel P. L., A. Peralta-Castro, N. Baruch-Torres, A. Fuentes-Pascacio, J. A. Pedroza-
845 García, *et al.*, 2021 Arabidopsis thaliana PrimPol is a primase and lesion bypass
846 DNA polymerase with the biochemical characteristics to cope with DNA damage in
847 the nucleus, mitochondria, and chloroplast. Sci. Rep. 11: 20582.

848 Golin S., Y. L. Negroni, B. Bennewitz, R. B. Klösgen, M. Mulisch, *et al.*, 2020 WHIRLY2 plays
849 a key role in mitochondria morphology, dynamics, and functionality in Arabidopsis
850 thaliana. Plant Direct 4: e00229.

851 Gualberto J. M., and K. J. Newton, 2017 Plant Mitochondrial Genomes: Dynamics and
852 Mechanisms of Mutation. Annu. Rev. Plant Biol. 68: 225–252.

853 Handa H., 2003 The complete nucleotide sequence and RNA editing content of the
854 mitochondrial genome of rapeseed (Brassica napus L.): comparative analysis of the
855 mitochondrial genomes of rapeseed and Arabidopsis thaliana. Nucleic Acids Res.
856 31: 5907–5916.

857 Haradhvala N. J., P. Polak, P. Stojanov, K. R. Covington, E. Shinbrot, *et al.*, 2016 Mutational
858 Strand Asymmetries in Cancer Genomes Reveal Mechanisms of DNA Damage and
859 Repair. Cell 164: 538–549.

860 Huang C. Y., N. Grünheit, N. Ahmadinejad, J. N. Timmis, and W. Martin, 2005 Mutational
861 decay and age of chloroplast and mitochondrial genomes transferred recently to
862 angiosperm nuclear chromosomes. Plant Physiol. 138: 1723–1733.

863 Itsara L. S., S. R. Kennedy, E. J. Fox, S. Yu, J. J. Hewitt, *et al.*, 2014 Oxidative stress is not a
864 major contributor to somatic mitochondrial DNA mutations. PLoS Genet. 10:
865 e1003974.

866 Kaplanis J., N. Akawi, G. Gallone, J. F. McRae, E. Prigmore, *et al.*, 2019 Exome-wide
867 assessment of the functional impact and pathogenicity of multinucleotide
868 mutations. Genome Res. 29: 1047–1056.

869 Kennedy S. R., J. J. Salk, M. W. Schmitt, and L. A. Loeb, 2013 Ultra-sensitive sequencing
870 reveals an age-related increase in somatic mitochondrial mutations that are
871 inconsistent with oxidative damage. PLoS Genet. 9: e1003794.

Kennedy S. R., M. W. Schmitt, E. J. Fox, B. F. Kohrn, J. J. Salk, *et al.*, 2014 Detecting ultralow-frequency mutations by Duplex Sequencing. Nat. Protoc. 9: 2586–2606.

Kubo T., and K. J. Newton, 2008 Angiosperm mitochondrial genomes and mutations. Mitochondrion 8: 5–14.

Li H., 2018 Minimap2: pairwise alignment for nucleotide sequences. Bioinformatics 34: 3094–3100.

Liu Y., B. Zhou, A. Khan, J. Zheng, F. U. Dawar, *et al.*, 2021 Reactive Oxygen Species Accumulation Strongly Allied with Genetic Male Sterility Convertible to Cytoplasmic Male Sterility in Kenaf. Int. J. Mol. Sci. 22. https://doi.org/10.3390/ijms22031107

Lu Z., J. Cui, L. Wang, N. Teng, S. Zhang, *et al.*, 2021 Genome-wide DNA mutations in Arabidopsis plants after multigenerational exposure to high temperatures. Genome Biol. 22: 160.

Martínez-Zapater J. M., P. Gil, J. Capel, and C. R. Somerville, 1992 Mutations at the Arabidopsis CHM locus promote rearrangements of the mitochondrial genome. Plant Cell 4: 889–899.

Miller-Messmer M., K. Kühn, M. Bichara, M. Le Ret, P. Imbault, *et al.*, 2012 RecA-dependent DNA repair results in increased heteroplasmy of the Arabidopsis mitochondrial genome. Plant Physiol. 159: 211–226.

Moeckel C., A. Zaravinos, and I. Georgakopoulos-Soares, 2023 Strand asymmetries across genomic processes. Comput. Struct. Biotechnol. J. 21: 2036–2047.

Mower J. P., D. B. Sloan, and A. J. Alverson, 2012 Plant Mitochondrial Genome Diversity: The Genomics Revolution, pp. 123–144 in *Plant Genome Diversity Volume 1: Plant Genomes, their Residents, and their Evolutionary Dynamics*, edited by Wendel J. F., Greilhuber J., Dolezel J., Leitch I. J. Springer Vienna, Vienna.

Mugal C. F., H.-H. von Grünberg, and M. Peifer, 2009 Transcription-induced mutational strand bias and its effect on substitution rates in human genes. Mol. Biol. Evol. 26: 131–142.

Negroni Y. L., I. Doro, A. Tamborrino, I. Luzzi, S. Fortunato, *et al.*, 2024 The Arabidopsis Mitochondrial Nucleoid-Associated Protein WHIRLY2 Is Required for a Proper Response to Salt Stress. Plant Cell Physiol. 65: 576–589.

Palmer J. D., and L. A. Herbon, 1988 Plant mitochondrial DNA evolves rapidly in structure, but slowly in sequence. J. Mol. Evol. 28: 87–97.

Peñafiel-Ayala A., A. Peralta-Castro, J. Mora-Garduño, P. García-Medel, A. G. Zambrano-Pereira, *et al.*, 2023 Plant organellar MSH1 is a displacement loop specific endonuclease. Plant Cell Physiol. https://doi.org/10.1093/pcp/pcad112

Pérez Di Giorgio J. A., É. Lepage, S. Tremblay-Belzile, S. Truche, A. Loubert-Hudon, *et al.*, 2019 Transcription is a major driving force for plastid genome instability in Arabidopsis. PLoS One 14: e0214552.

Pucker B., D. Holtgräwe, K. B. Stadermann, K. Frey, B. Huettel, *et al.*, 2019 A chromosome-level sequence assembly reveals the structure of the Arabidopsis thaliana Nd-1 genome and its gene set. PLoS One 14: e0216233.

Quinlan A. R., and I. M. Hall, 2010 BEDTools: a flexible suite of utilities for comparing genomic features. Bioinformatics 26: 841–842.

Rowan B. A., D. J. Oldenburg, and A. J. Bendich, 2010 RecA maintains the integrity of chloroplast DNA molecules in Arabidopsis. J. Exp. Bot. 61: 2575–2588.

Sanchez-Contreras M., M. T. Sweetwyne, B. F. Kohrn, K. A. Tsantilas, M. J. Hipp, *et al.*, 2021 A replication-linked mutational gradient drives somatic mutation accumulation and influences germline polymorphisms and genome composition in mitochondrial DNA. Nucleic Acids Res. 49: 11103–11118.

921 Sandor S., Y. Zhang, and J. Xu, 2018 Fungal mitochondrial genomes and genetic
922 polymorphisms. Appl. Microbiol. Biotechnol. 102: 9433–9448.

923 Shedge V., M. Arrieta-Montiel, A. C. Christensen, and S. A. Mackenzie, 2007 Plant
924 mitochondrial recombination surveillance requires unusual RecA and MutS
925 homologs. Plant Cell 19: 1251–1264.

926 Skippington E., T. J. Barkman, D. W. Rice, and J. D. Palmer, 2017 Comparative
927 mitogenomics indicates respiratory competence in parasitic Viscum despite loss of
928 complex I and extreme sequence divergence, and reveals horizontal gene transfer
929 and remarkable variation in genome size. BMC Plant Biol. 17: 1–12.

930 Sloan D. B., A. J. Alverson, J. P. Chuckalovcak, M. Wu, D. E. McCauley, *et al.*, 2012 Rapid
931 evolution of enormous, multichromosomal genomes in flowering plant
932 mitochondria with exceptionally high mutation rates. PLoS Biol. 10: e1001241.

933 Smith D. R., and P. J. Keeling, 2015 Mitochondrial and plastid genome architecture:
934 Reoccurring themes, but significant differences at the extremes. Proc. Natl. Acad.
935 Sci. U. S. A. 112: 10177–10184.

936 Stupar R. M., J. W. Lilly, C. D. Town, Z. Cheng, S. Kaul, *et al.*, 2001 Complex mtDNA
937 constitutes an approximate 620-kb insertion on Arabidopsis thaliana chromosome
938 2: implication of potential sequencing errors caused by large-unit repeats. Proc.
939 Natl. Acad. Sci. U. S. A. 98: 5099–5103.

940 Sun S., Q. Li, L. Kong, and H. Yu, 2018 Multiple reversals of strand asymmetry in molluscs
941 mitochondrial genomes, and consequences for phylogenetic inferences. Mol.
942 Phylogenet. Evol. 118: 222–231.

943 Vöhringer H., A. Van Hoeck, E. Cuppen, and M. Gerstung, 2021 Learning mutational
944 signatures and their multidimensional genomic properties with TensorSignatures.
945 Nat. Commun. 12: 3628.

946 Waneka G., J. M. Svendsen, J. C. Havird, and D. B. Sloan, 2021 Mitochondrial mutations in
947 Caenorhabditis elegans show signatures of oxidative damage and an AT-bias.
948 Genetics 219. https://doi.org/10.1093/genetics/iyab116

949 Waters C. A., N. T. Strande, J. M. Pryor, C. N. Strom, P. Mieczkowski, *et al.*, 2014 The fidelity
950 of the ligation step determines how ends are resolved during nonhomologous end
951 joining. Nat. Commun. 5: 4286.

952 Wei S.-J., M. Shi, X.-X. Chen, M. J. Sharkey, C. van Achterberg, *et al.*, 2010 New views on
953 strand asymmetry in insect mitochondrial genomes. PLoS One 5: e12708.

954 Wolfe K. H., W. H. Li, and P. M. Sharp, 1987 Rates of nucleotide substitution vary greatly
955 among plant mitochondrial, chloroplast, and nuclear DNAs. Proc. Natl. Acad. Sci.
956 U. S. A. 84: 9054–9058.

957 Wu Z., G. Waneka, A. K. Broz, C. R. King, and D. B. Sloan, 2020 MSH1 is required for
958 maintenance of the low mutation rates in plant mitochondrial and plastid genomes.
959 Proc. Natl. Acad. Sci. U. S. A. 117: 16448–16455.

960 Wu Z.-Q., X.-Z. Liao, X.-N. Zhang, L. R. Tembrock, and A. Broz, 2022 Genomic architectural
961 variation of plant mitochondria—A review of multichromosomal structuring. J. Syst.
962 Evol. 60: 160–168.

963 Wynn E. L., and A. C. Christensen, 2019 Repeats of Unusual Size in Plant Mitochondrial
964 Genomes: Identification, Incidence and Evolution. G3 9: 549–559.

965 Xiao-Ming Z., W. Junrui, F. Li, L. Sha, P. Hongbo, *et al.*, 2017 Inferring the evolutionary
966 mechanism of the chloroplast genome size by comparing whole-chloroplast
967 genome sequences in seed plants. Sci. Rep. 7: 1555.

968 Zampini É., É. Lepage, S. Tremblay-Belzile, S. Truche, and N. Brisson, 2015 Organelle DNA
969 rearrangement mapping reveals U-turn-like inversions as a major source of genomic
970 instability in Arabidopsis and humans. Genome Res. 25: 645–654.

971 Zou Y., W. Zhu, D. B. Sloan, and Z. Wu, 2022 Long-read sequencing characterizes
972 mitochondrial and plastid genome variants in Arabidopsis msh1 mutants. Plant J.
973 112: 738–755.